

P-Wave Arrival-Time Tomography of the Middle East Using ISC-EHB and Waveform Data

Ebru Bozdağ  * 1,2, Susini Desilva  2,3, Guust Nolet  4,5, Ridvan Örsvuran  1, Rengin Gök  6, Yahya M. Tarabulsi  7, Ahmed Hosny  7, Khalid Yousef  7, Abdullah Mousa  7

¹Department of Applied Mathematics & Statistics, Colorado School of Mines, Golden, CO, USA, ²Department of Geophysics, Colorado School of Mines, Golden, CO, USA, ³Columbus State Community College, Columbus, OH, USA, ⁴Université Côte d'Azur/CNRS/OCA/IRD, Géoazur, Sophia Antipolis, France, ⁵Department of Geosciences, Princeton University, Princeton, NJ, USA, ⁶Lawrence Livermore National Laboratory, Livermore, CA, USA, ⁷Saudi Geological Survey, National Program for Earthquakes and Volcanos, Jeddah, Saudi Arabia

Author contributions: *Conceptualization:* EB. *Methodology:* GN. *Software:* GN. *Validation:* SD, GN, EB. *Formal Analysis:* SD, EB, GN. *Investigation:* EB, SD, GN, RG, RÖ. *Resources:* EB, GN, RG, YT, AH, KY, AM. *Writing - Original draft:* EB, SD. *Writing - Review & Editing:* EB, SD, GN, RG, YT, AH, KY, AM. *Visualization:* SD, RÖ, EB. *Supervision:* EB, GN. *Funding acquisition:* EB.

Abstract High-resolution seismic images are essential to gain insights into tectonic and geodynamical processes and assess seismic hazards. We constructed a P-wave model, MEPT (Middle East P-wave Travel-time), of the upper mantle beneath the Middle East and the surrounding region, which has a complex tectonic and geological history embodying various plate boundaries such as spreading ridges, subduction, suture zones, and strike-slip faults causing destructive earthquakes, specifically in Iran, Caucasus and Anatolia, and active volcanism. We use data from the ISC-EHB bulletin and onset-time readings of first-arrival P waves from waveforms recorded in the Arabian Peninsula. The additional onset-time readings from the regional waveform data significantly improve the resolution of the structure underneath the Arabian Peninsula, clearly indicating the boundary between the Arabian platform and the Arabian shield down to about 300 km depth, highlighted by slow and fast wavespeed perturbations in the upper mantle. Consistent with previous studies, we observe the Arabian-Eurasian collision, the Red Sea rifting, the Hellenic Arc, and low-velocity anomalies beneath the lithosphere of the Red Sea and the west of the Arabian shield. Our model supports the connection of the slow wavespeed anomalies in the lithosphere along the Red Sea to the Afar plume and shows evidence for smaller mantle upwellings underneath the Arabian plate and Jordan.

Production Editor:
Carmine Galasso
Handling Editor:
Suzan van der Lee
Copy & Layout Editor:
Ethan Williams

Received:
3 April 2024
Accepted:
17 April 2025
Published:
23 June 2025

1 Introduction

The Middle East and the surrounding region, including Anatolia and the Caucasus, are forged by the amalgamation of different geological units and actively evolve through various plate boundaries and fault systems (Fig. 1). The GPS studies show $\sim 20 - 30$ mm/year counterclockwise rotation of the Arabian plate and its adjoining areas of Iran, Turkey, the Aegean Sea, and the Peloponnese Peninsula with respect to the Eurasian plate, explaining the deformation related to the continental interaction of the African, Arabian and Eurasian plates (e.g., McClusky et al., 2000; Reilinger et al., 2006; Le Pichon and Kreemer, 2010; Viltres et al., 2022). The Bitlis-Zagros suture zone is one of the most remarkable tectonic features related to the collision after the closing of the Tethys Ocean. This broad rotational movement is accompanied by the subduction along the Hellenic-Cyprus trench system in the Mediterranean, the crustal spreading at the Eastern African rift system, and the ocean-floor spreading at the Red Sea and Gulf of Aden rift systems. The slab rollback (e.g., Bozkurt, 2001; Ring et al., 2010) along the Hellenic Arc facilitates the extensional regime at Aegean and Western Anatolia. The

compressional forces deriving from the collision of the Arabian plate on the East associated with the closing of the Neo-Tethys ocean (e.g., Agard et al., 2005; Hatzfeld and Molnar, 2010) influences active dynamics of the strike-slip North and East Anatolian faults resulting in westward escape and the counterclockwise rotational movement of the Anatolian plate (e.g., Şengör et al., 1985; Reilinger et al., 2006; Sonder and England, 1989; Rovden, 1993).

The Arabian shield borders with the Red Sea on the East, one of the very slow-spreading centers on Earth whose tectonic structure is still actively debated. One of the main challenges of the geophysical data from the Red Sea (e.g., seismic, gravity, magnetic) is the thick sediment layer and the salt bodies, which complicate measurements and make the observation of ridge signature and mapping transform faults difficult (e.g., Augustin et al., 2021; Parisi et al., 2024). While some studies suggest that the Red Sea might still be in the transition between continental rifting to oceanic spreading (e.g., Bonatti, 1985; Schettino et al., 2016; Artemieva et al., 2022), although there is no consensus on the age, there is evidence from geophysical data that the Red Sea completed its rifting phase becoming a mature oceanic basin 5-13 million years ago (e.g., Augustin et al., 2021).

*Corresponding author: bozdag@mines.edu

Some models of the Red Sea suggest the oceanic crust was created all the way from the South to the Sinai (e.g., Augustin et al., 2021; Delaunay et al., 2024) while the spreading along the ridge is more on the southern part with limited extension to the north (e.g., Coleman and McGuire, 1988; Almalki et al., 2015). The evolution of the Red Sea is also crucial to understanding the volcanism in the Arabian Peninsula and its surroundings. Within the same context, the cause of the rifting on the Red Sea is the subject of debate. Strains can be caused by several candidate forces active today: the rotation of the Arabian plate, its possible subduction underneath Zagros, or changes in the plate motion after subduction of the Neo-Tethys slowed down in the Western Mediterranean (Reilinger and McClusky, 2011). Rifting might be caused by mantle upwelling of which the origin is also uncertain, such as the connection to the Afar plume with a deeper upwelling (e.g., Montelli et al., 2004) or its connection with Neogene volcanism from a mantle plume beneath Jordan (Chang and Van der Lee, 2011) and with collision-related volcanism as far north as Turkey (Sen et al., 2004). Khrepy et al. (2021), using data from the Egyptian and Saudi networks, suggest the Harrats (basaltic fields) may be fed from a plume-like feature.

The interaction of multiple plates driven by major boundary types (i.e., transform, subduction, divergent, collision) makes the area, extending from Anatolia to the Caucasus to Iran, one of the most seismically hazardous regions on Earth with frequent and devastating earthquakes (e.g., Giardini et al., 1993; Shedlock et al., 2000). Seismicity (e.g., Nissen et al., 2011, 2014), seismic hazard assessment (e.g., Giardini et al., 2018; Kiuchi et al., 2019) and regional source mechanisms and locations (e.g., Adams et al., 2009; Gök et al., 2016; Karasözen et al., 2016, 2019; Chiang et al., 2021) provide the foundation for arranging strategic means of mitigating earthquake-related damage. However, the characterization of seismic sources along complex tectonic boundaries, such as the Hellenic trench system and Zagros suture belt, has shown to be challenging and prone to large uncertainties (e.g., Engdahl et al., 2006; Braunmiller and Nábělek, 1996; Braunmiller et al., 2002) due to the uncertainties in structural models. Therefore, higher-resolution crustal and upper-mantle seismic models of the subduction/rifting history embedded within the lithosphere are crucial to reducing uncertainties in source mechanism estimates and improving our depiction of the behavior of conglomerate fault systems in the region.

The seismic activity in the study region is also complemented by active volcanism. The Harrats, located west of the Arabian plate, is the largest lava field in the area. Yet, their origin is still an ongoing debate similar to the opening of the Red Sea discussed above (e.g., Ball et al., 2023). The proximity of Harrats to the Red Sea and their alignment is one of the potential explanations for their origin related to the rifting process. One of the main theories on the cause of rifting is the Afar plume, which coincides with the Cenozoic magmatism in East Africa. The volcanic provinces on the western Arabian plate and in the northwest at Jordan are gener-

ally explained by the channelization of the Afar plume northward along the Red Sea (e.g., Camp and Roobol, 2006; Duncan et al., 2016) or smaller regional mantle plumes underneath the Arabian plate and Jordan (e.g., Weinstein et al., 2006; Chang and Van der Lee, 2011) and a sheet of mantle upwelling along the Red Sea connected to the Afar plume (e.g., McKenzie, 2020). Another theory is also related to the melting due to the decompression generated by the lithospheric thinning in response to the rifting of the Red Sea (e.g., Sanfilippo et al., 2019). The volcanic fields have been associated with scattered occurrences of earthquake swarms (e.g., Pallister et al., 2010; Mukhopadhyay et al., 2013) and about 21 known volcanic eruptions over the last 1,500 years (Camp et al., 1987). The last eruption in the southern section of the Arabian shield was in 1937 in Yemen, while that in the northern section was in 1256 AD in northwest Saudi Arabia (Camp et al., 1987). Understanding source characteristics of smaller magnitude events, such as the 2009 earthquake swarms in the volcanic fields in the northwest of Saudi Arabia (e.g., Chiang et al., 2021), and rifting dynamics in the upper mantle beneath the Red Sea region is also necessary to better assess the geodynamics of the driving mechanisms leading to episodic magma intrusions of the region (e.g., Civilini et al., 2019).

One of the main concerns for seismic source characterization for earthquakes and any other seismic sources in the region is the 3D effect of complex geological structures such as the East Anatolian-Zagros plateau that is abundant with active faults, volcanism, and highly variable topographic structures (e.g., Tavakoli and Ghafory-Ashtiany, 1999; Pasyanos et al., 2001, 2021) on seismic wave propagation. Detailed seismic models of the lithosphere and the upper mantle are essential to understanding the evolution and dynamics of closely related multi-plate movement within the Middle East from a perspective of geological interest and provide a solid basis for tectonic-related hazard risk assessments. Global seismic tomographic models, based on body waves (e.g., Bijwaard et al., 1998), surface waves (e.g., Trampert et al., 2004), S and surface-wave waveforms (e.g., Li and Romanowicz, 1996; Schaeffer and Lebedev, 2013), a combination of multiple data sets (e.g., Ritsema et al., 2011) and recent adjoint waveform models (e.g., Lei et al., 2020) are overall compatible to explain the general large-scale tectonics of the region regardless of data types or inversion strategies. Regionally focused tomographic studies have been able to address finer structures such as the Zagros collision zone (e.g., Maggi and Priestley, 2005; Kaviani et al., 2007; Simmons et al., 2012; Wei et al., 2019), the structure beneath Anatolia (e.g., Al-Lazki et al., 2004; Zhu et al., 2012), the Red Sea rifting connected to the Arabian shield (Chang and Van der Lee, 2011; Park et al., 2008; Kaviani et al., 2020) and the Arabian platform basement which is covered by thick sediments (e.g., Gök et al., 2007).

Imaging the subsurface beneath the Middle East at the continental scale is challenging because of the unevenly distributed source and stations and sparse data coverage, mainly in the Arabian Peninsula. Recent

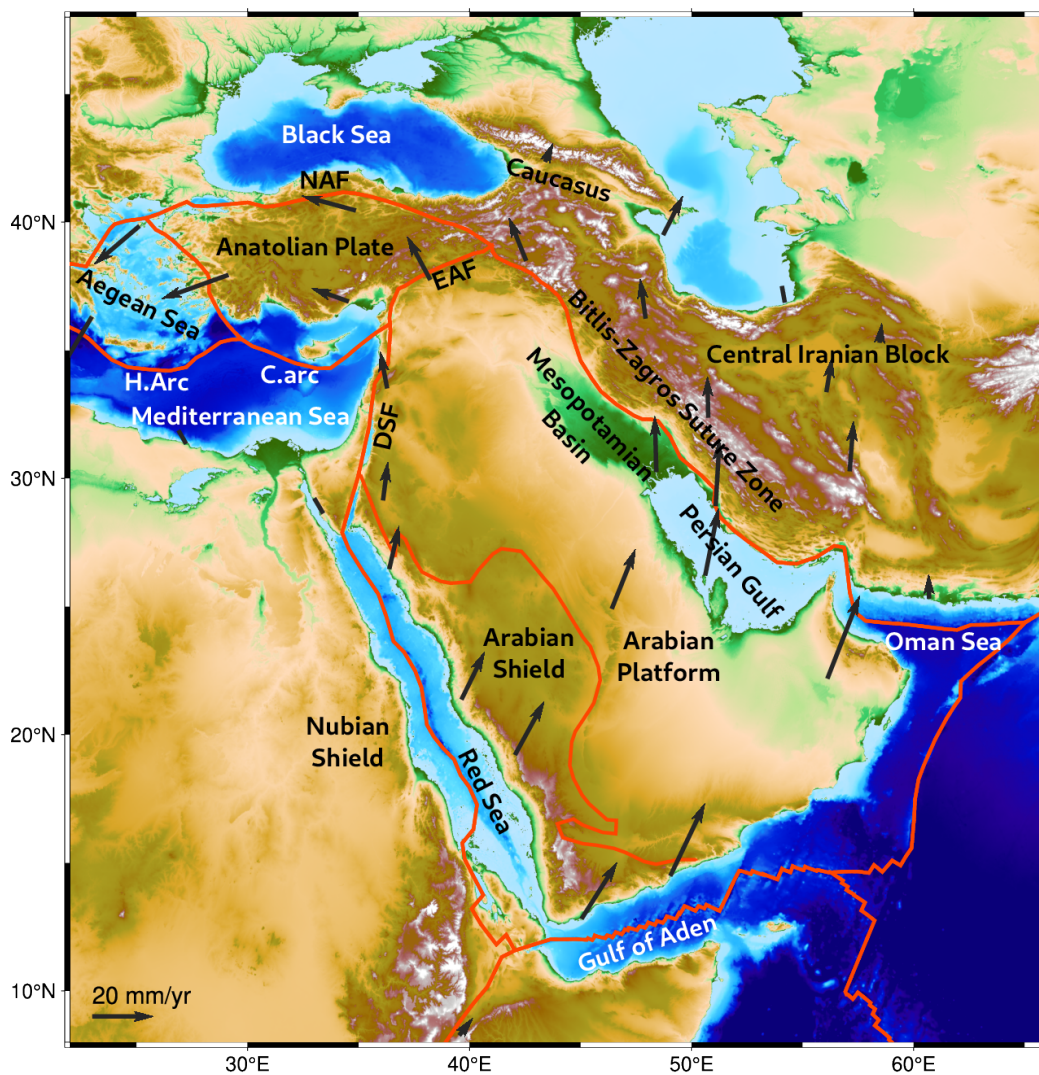


Figure 1 Topographic map of the study region with major tectonic units. NAF: North Anatolian Fault, EAF: East Anatolian Fault, DSF: Dead Sea Fault, H. Arc: Hellenic Arc, C. Arc: Cyprus Arc. Black arrows denote GPS velocities relative to Eurasia (Reilinger et al., 2006). Red lines indicate plate boundaries (Bird, 2003) and the boundary between the Arabian shield and the Arabian platform (Mokhtar and Al-Saeed, 1994). The scale for GPS vectors is shown on the bottom left.

studies in the region have taken advantage of the increasing amount of seismic data throughout the region and provide higher resolution tomographic images using regional body and surface waves to investigate the lithospheric structure and tectonic evolution (e.g., Al-Damegh et al., 2004; Tkalčić et al., 2006; Hansen et al., 2007, 2008; Tang et al., 2016, 2018, 2019; Kim et al., 2023; Kaviani et al., 2020; Pasyanos et al., 2021; Lim et al., 2020; Celli et al., 2020). The regional models for the Arabian Peninsula typically focus on the shear-wavespeed models where surface waves can complement S waves to improve the coverage (i.e., Chang et al., 2012). Chang et al. (2012) then constructed a P-wavespeed model derived from their S-wavespeed model by using the scaling relationships between P and S waves. Celli et al. (2020) jointly inverted P and S wavespeeds in a surface-wave tomography study of the African continent, including the Middle East, which imaged the long-wavelength structure of our study region. Other long-wavelength P-wavespeed models of the region are coming from global traveltime (e.g., Simmons et al., 2021) and global adjoint

models, where P and S wavespeed models are jointly inverted (e.g., Bozdağ et al., 2016; Lei et al., 2020). Anatolian structure was inverted as part of the European tomographic studies (e.g., Zhu et al., 2012) and a recent adjoint tomography model of the Middle East region by Rodgers et al. (e.g., 2024) or separately based on teleseismic P-wave tomography (e.g., Biryol et al., 2011). Nevertheless, the P-wave resolution is still an ongoing challenge in seismic tomography, which is exacerbated by the sparse data coverage and limited surface-wave contribution compared to S-wave models.

In this study, we present the P-wave model **MEPT** (Middle East P-wave Traveltime) of the Middle East and the surrounding region, performing an arrival-time tomography with an improved data coverage based on the ISC-EHB Bulletin (Engdahl et al., 2020) published by the International Seismological Centre and hereafter referred to as “ISC” (International Seismological Centre, 2020) and onset-time readings of the first-arrival P waveforms of regional earthquakes recorded in the Arabian Peninsula. Our ISC data involves more recent and

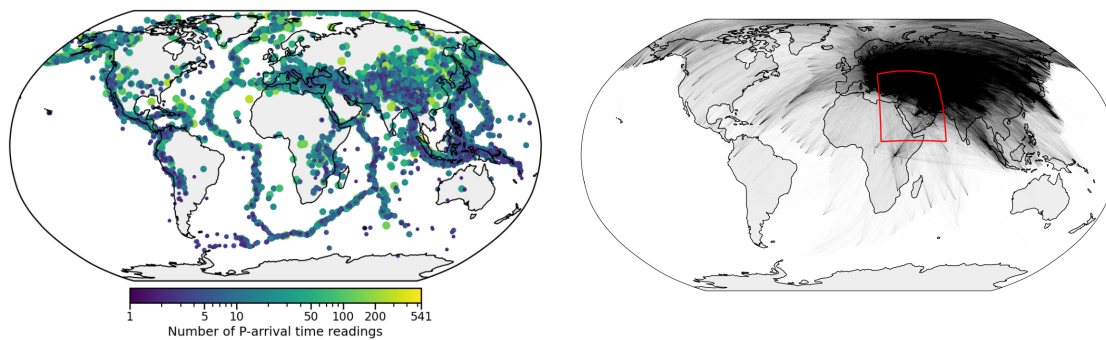


Figure 2 Distribution of the number of P-wave arrival-time readings per event from the ISC catalog (*left*) and the corresponding 300,513 great-circle ray paths (*right*) used in this study. The red box on the right map shows the study region.

well-located arrival times, including teleseismic events, within the period range of 1990 – 2016 compared to earlier P-wave models of the region by, for instance, Sandvol et al. (1998); Al-Lazki et al. (2004); Park et al. (2007); Simmons et al. (2012); Wei et al. (2019). Following studies such as Chang and Van der Lee (2011), which combine S-wave ISC arrival times with those from S waveforms to enhance images of the upper mantle beneath the western side of the Middle East, in this study, we combine P-wave arrival times from the ISC catalog with the onset-time readings of the first-arrival P waveforms recorded by the seismic stations operated by the Saudi Geological Survey (SGS). A part of the SGS stations (i.e., the Saudi National Seismic Network, SNSN) was also used in some previous studies (i.e., Khrepy et al., 2021; Hansen et al., 2008).

The paper is structured as follows. We first give brief information about the data from the ISC catalog and onset-time readings from waveforms used in our inversions, followed by the tomography technique. In Section 3, we present our models constructed based on ISC data only and ISC data combined with onset-time readings from waveform data from the Arabian Peninsula. In Section 4, we discuss our observations in the context of the region’s tectonics and the previous tomographic models. Finally, we summarize our results and observations in Conclusions in Section 5.

2 Data and Method

In this section, we provide some background information about our dataset, which combines P-wave arrival times from the ISC catalog with first-arrival P-wave onset-time readings made on waveform data from 110 regional events recorded by seismic stations in the Arabian Peninsula, and our arrival-time tomography technique.

2.1 ISC dataset

In our inversions, we use P-wave arrival-time data from the ISC catalog of globally distributed earthquakes that occurred between 1990 – 2016. We select earthquakes with at least 50 P-wave onset-time picks recorded worldwide. We ensure that no two selected events were closer than 20 km to limit cluttered ray paths from events lo-

cated in regions with high seismic activity. Another criterion set is to pick not more than 40 ray paths per corridor (see the corridor definition in the Supplementary Material, Fig. S1) and select data to balance the ray coverage as best as possible. In addition, we select picks listed in the catalog with at least two decimal precision. The resultant ISC dataset consists of a total of 16,264 global events fitting our criteria, leading to 300,513 P-wave onset-time picks out of a total of ~ 19 million in the ISC catalog within our time period, recorded by a total of 1,114 stations located in our study region. The epicentral distribution of the selected events, the representation of how many P-wave picks we have for each of them and the associated great-circle ray paths are shown in Fig. 2. On the left panel of Fig. 3, we illustrate how many picks were collected at each seismic station in our study area from the ISC catalog where the sparsity of data coverage is clearly seen in the Arabian Peninsula.

2.2 First-arrival P-wave onset-time readings from waveform data

We gather waveform data from 110 regional earthquakes between 2007 – 2020 recorded by the seismic network operated by the SGS in the Arabian Peninsula. We carefully pick 2,916 onset times from the first-arrival P waves on the vertical component of the waveform data set. On the right panel of Fig. 3, we show the distribution of P-wave arrival times from the ISC catalog combined with the onset-time readings from waveforms recorded on the Arabian Peninsula. After regular data processing steps applied to the waveform data (i.e., updating headers with event and station information, removing the trend and the mean, bandpass filtering), we apply 10 s time window around the estimated ray-theoretical arrival times of first-arrival P waves based on our 1D reference model AK135 (Kennett et al., 1995). We manually pick the onset times of the first-arrival P waves and calculate the ‘P-wave delay time’ of each trace as the difference between our picked onset times and corresponding AK135 estimations. Note that we use the ISC event information in this procedure, which pertains to the first motion of the fault, to be consistent with our ISC database. Waveforms are bandpass filtered between 0.5 Hz – 2.0 Hz with a 6-pole Butterworth filter to ensure

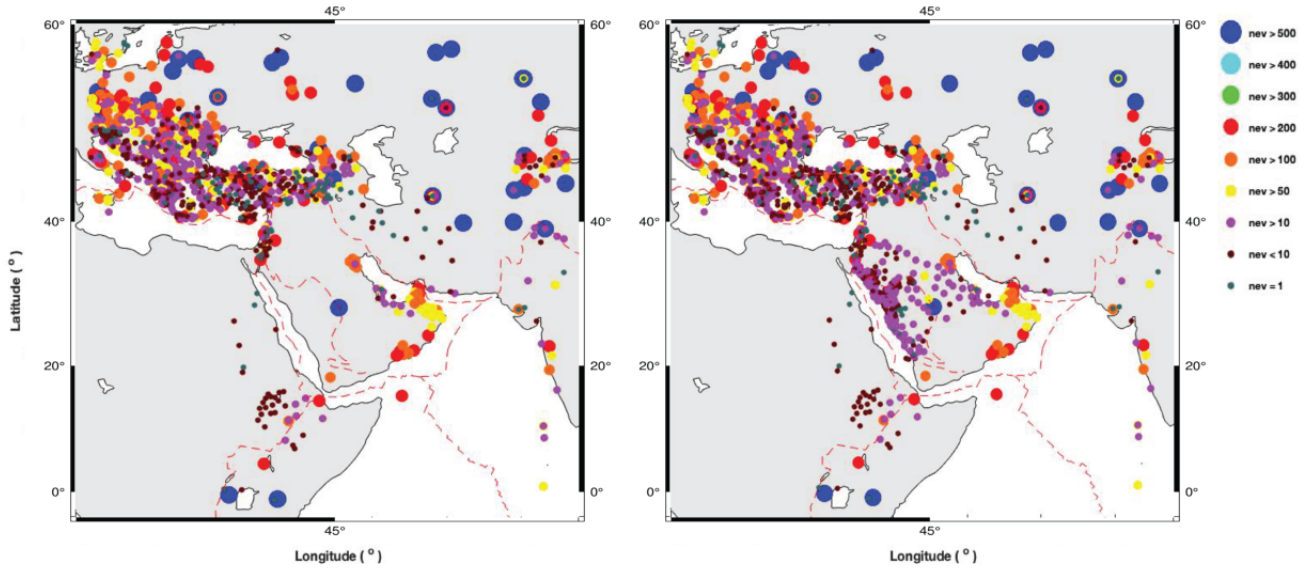


Figure 3 *Left:* Distribution of P-wave arrival times from the global ISC catalog recorded by the stations in the study area. *Right:* Same as the figure on the *left* but with the addition of the onset-time readings from the waveform data recorded by the SGS network on the Arabian Peninsula.

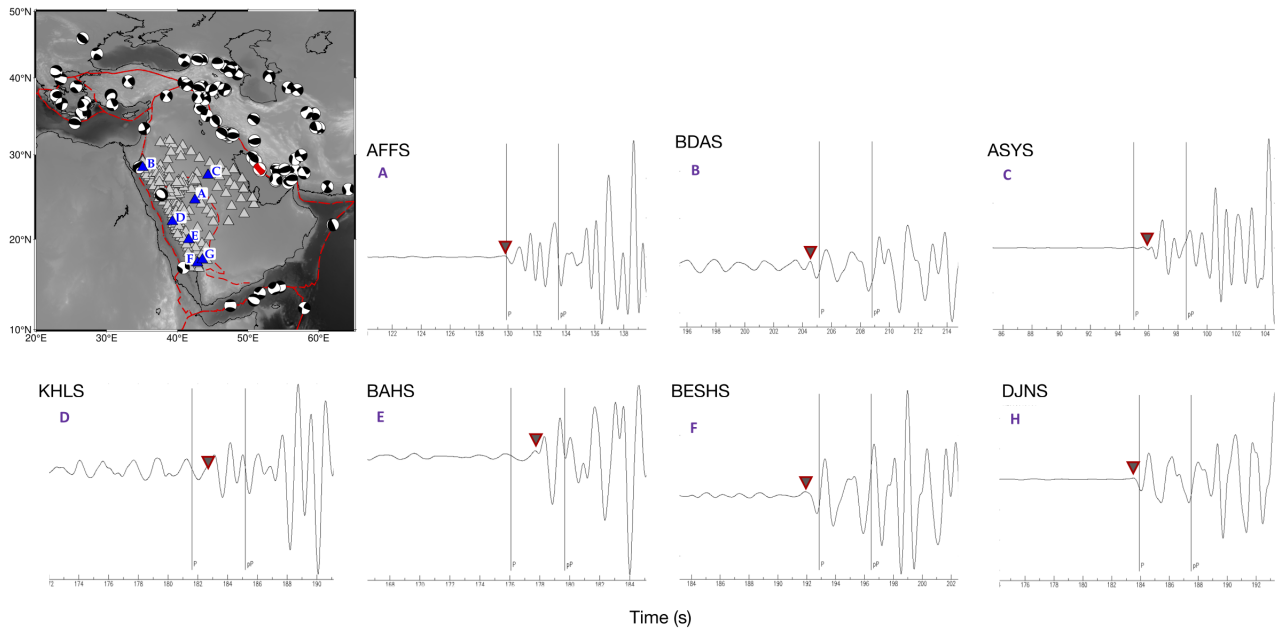


Figure 4 Vertical-component seismograms recorded at sample SGS stations (triangles on the map) on the Arabian Peninsula for the 2013 Southern Iran earthquake ($M_w = 6.4$, depth= 12 km) shown by the red beachball. Plotted seismograms are recorded by the blue triangles on the map. Vertical lines on the seismograms denote the AK135(Kennett et al., 1995) ray theoretical predictions of the first-arrival P waves. Inverted triangles on the seismograms show the picked P-wave arrival times. Time delay input for the inversion is then defined as the picked arrival times with respect to AK135 predictions.

sharp onset times distinguishable from preceding noise after experimenting with various other filters (i.e., combinations of causal/zero-phase filtering at different frequency bands tested within the range of 0.2 Hz – 4 Hz) including the sharp high-pass causal filter used by Nolet et al. (2019) tested with cutoff frequencies in the range of 0.25 Hz – 0.5 Hz. Sample vertical-component seismograms from a regional earthquake in Iran recorded by a set of seismic stations in the Arabian Peninsula with our

first-arrival P-wave onset-time picks are shown in Fig. 4.

2.3 P-wave arrival-time tomography

The depth sections of the ray density of our dataset, including the ISC data and the onset-time readings from the waveform data in the Arabian Peninsula, the lithosphere and mantle down to 1,400 km are presented in Fig. 5. Since we assimilate onset-time readings of waveform data from regional earthquakes, the main im-

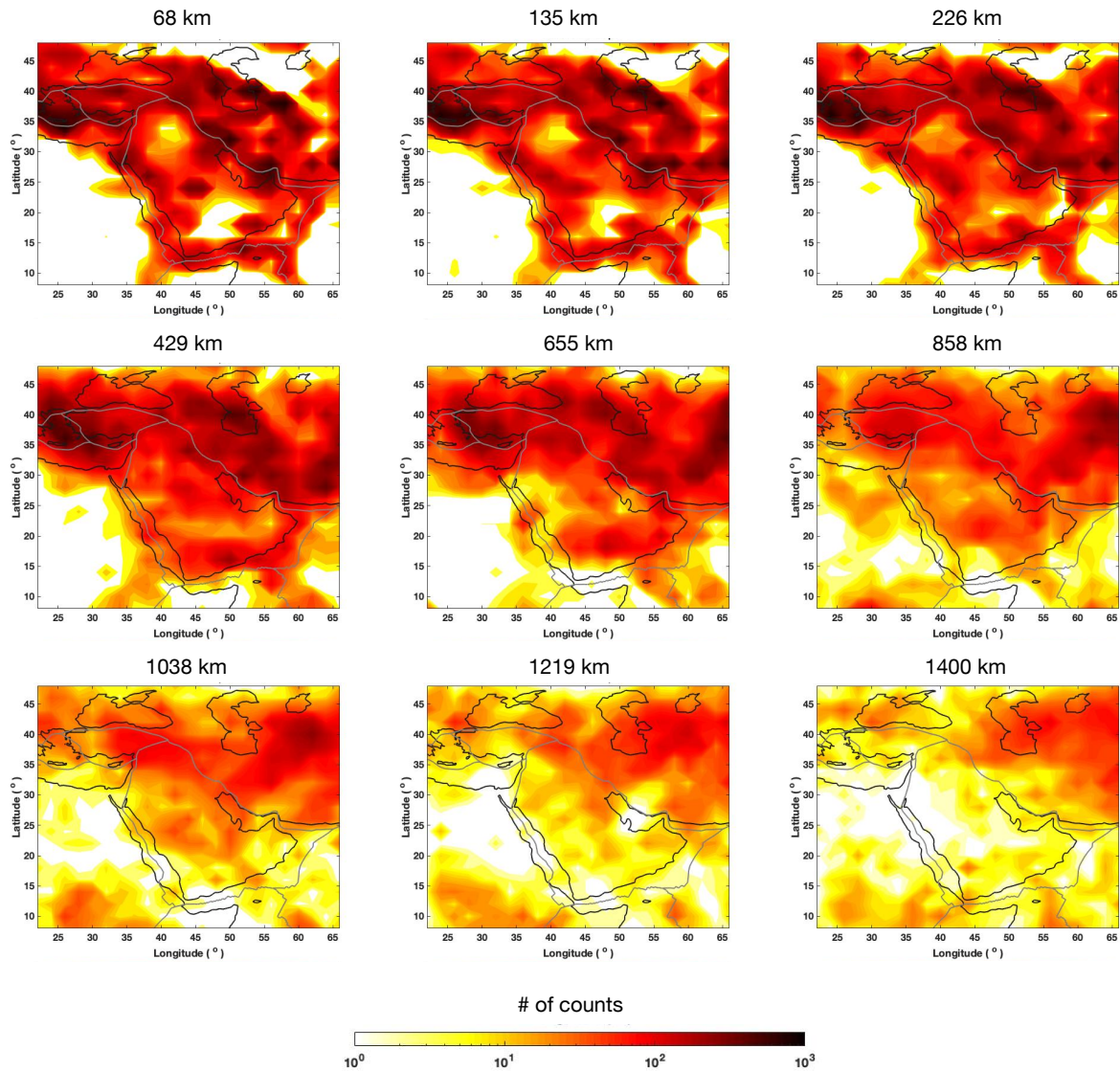


Figure 5 Density of hit counts of ray paths used in the inversion, including the onset-time readings from the SGS stations in the Arabian Peninsula at every $2^\circ \times 2^\circ$ cells shown at various depths.

provement in data coverage is observed in the lithosphere down to $\sim 350 - 400$ km underneath the Middle East.

In this study, we use the traveltimes inversion software package *BD-soft* (Nolet, 2008) based on ray theory to invert for the compressional P-wavespeed perturbations with respect to the 1D reference model AK135 (Kennett et al., 1995). Since we use onset-time readings, ray theory should be valid where the first-order scattering effects can be neglected. To the first order, perturbations are defined as $\delta V_p = \Delta V_p / V_p^0$, where V_p and V_p^0 are the P wavespeeds in 3D and 1D models, respectively, and $\Delta V_p = V_p - V_p^0$. For the inverse problem we aim to obtain model parameters $m_i = (\frac{\Delta V_p}{V_p^0})_i$ defined on a cubed-Earth grid (Charley et al., 2013) which has ~ 70 km size volume pixels (voxels) on the surface with a total of ~ 3.6 million voxels covering the globe from surface to the core-mantle boundary (CMB). The observed P-wave delay times, i.e., the difference between observed and estimated P-wave arrival times by the 1D reference model AK135, are as-

signed to d_i , the elements of the data vector \mathbf{d} . Then the traveltimes sensitivity-kernel matrix, \mathbf{A} , is computed by a 1D ray tracing algorithm. The 3D crustal model Crust2.0 (Bassin et al., 2000) is used to correct the crustal perturbations by superimposing it onto AK135, which is used as the background model during the inversions. In addition, the ellipticity correction is applied to the data similar to Tian et al. (2007) and Nolet (2008).

We perform a ray-based linearized inversion to construct a P-wave model of the study region with a set of linear equations

$$\mathbf{A}\mathbf{m} = \mathbf{d}, \quad (1)$$

where \mathbf{m} and \mathbf{d} denote the $N \times 1$ model and $M \times 1$ data vectors, respectively, and \mathbf{A} is the $M \times N$ Jacobian matrix involving the partial derivatives of data with respect to model parameters. We perform a damped-least square inversion where model parameters are es-

timated such that

$$\mathbf{m} = (\mathbf{A}^T \mathbf{C}_d^{-1} \mathbf{A} + \gamma \mathbf{I})^{-1} \mathbf{A}^T \mathbf{C}_d^{-1} \mathbf{d}, \quad (2)$$

where \mathbf{C}_d is the diagonal data covariance matrix, γ is the damping factor and \mathbf{I} is the unit matrix. We then solve the following system of linear equations (Nolet et al., 2019)

$$\begin{pmatrix} \mathbf{A} \\ \epsilon_n \mathbf{I} \\ \epsilon_s \mathbf{D} \end{pmatrix} S^r \mathbf{y} = \begin{pmatrix} \mathbf{d} \\ 0 \\ 0 \end{pmatrix}, \quad (3)$$

followed by

$$\mathbf{m} = S \mathbf{y}, \quad (4)$$

where \mathbf{D} has second order differences between model parameters, while ϵ_n and ϵ_s are the weights for norm damping and smoothing, respectively. As in Nolet et al. (2019), we also use one or two relaxation steps (represented by S^r) as preconditioners to smooth the solution towards one that satisfies $\nabla^2 m = 0$ where we fix the ratio ϵ_n/ϵ_s . Figs. S5-S10 show how reduced χ^2 depends on the number of relaxation steps (r) and a damping parameterized by epsfac , $\epsilon_n = (\text{epsfac}) \times 30/(1 - \text{epsfac})$. We vary epsfac in a range of 0.0 - 1.0 to control the damping level from no-damping to high damping.

We derive error estimates for our arrival-time residuals using the method of Voronin et al. (2014) and its variant described by Nolet et al. (2019). For the onset time readings from the waveform data, we perform a manual selection excluding noisy data and traveltimes shifts compared to AK135 that do not fit our ISC data standard deviations as explained in Nolet and van der Lee (2022).

3 Results

To better understand the value of the arrival-time data from waveforms, we performed two sets of iterations: 1) with ISC data only and 2) with ISC data combined with the onset-time readings from waveforms recorded by the SGS network deployed on the Arabian Peninsula. Here, we present our results obtained by the assimilation of the ISC data with those from waveforms in the inversion, selected based on our checkerboard and L-curve tests. The readers are referred to the Supplementary Material for additional information including the inversion results with the ISC data only, vertical sections of the checkerboard tests for the ISC data with arrival-time readings from waveforms and the detailed L-curve tests.

In Figs. 6 and 7, we present the checkerboard tests of $4^\circ \times 4^\circ$ and $2.4^\circ \times 2.4^\circ$ cubed-checkers, respectively, with 4% P-wavespeed perturbations performed with our complete dataset (i.e., ISC data with onset-time readings from waveforms) to understand the potential resolution of our data coverage. The checkerboard tests of $4^\circ \times 4^\circ$ resolution show that overall, we have good resolution down to 1,400 km, which is best below ~ 400 km down to ~ 1200 km covering a region including the western part of the Red Sea. Although the resolution decreases around 1,200 km, we observe good resolution in Anatolia, the Arabian Peninsula, and Iran. The $2.4^\circ \times 2.4^\circ$

resolution checkerboard test results show the best resolution from ~ 400 km down to ~ 800 km where smearing occurs toward southwest below ~ 800 km. In the lithosphere, the resolution is promising, while there is a gap in resolution north of the Gulf of Aden. Overall, the additional arrival-time readings from waveforms significantly improve the resolution in the lithosphere of the Arabian Peninsula (see Figs. S3-S4 for the checkerboard results with the ISC data only). The vertical sections from $2.4^\circ \times 2.4^\circ$ checkerboard tests (Figs. S5-S6) are consistent with observations on the horizontal sections and show good resolution down to ~ 600 km wherever we have good data coverage, which is reduced in the south of the Arabian Peninsula and the west of the Red Sea. The additional data from waveforms, however, does not make much observable difference for depths below ~ 429 km. We do not see significant improvement in our model below the lithosphere for two reasons: 1) our ISC coverage is already good enough in the upper mantle because of the global dataset, 2) we use P-wave arrival-time readings of waveforms from local earthquake-receiver pairs where maximum epicentral distance is $\sim 17^\circ$ with corresponding turning points at ~ 410 km depth in model AK135 (see Fig. S13 for the data count histogram as a function of epicentral distance). The checkerboard tests suggest that our P-wave model has the best resolution in the upper mantle and can resolve $2.4^\circ \times 2.4^\circ$ structure in the Arabian Peninsula as well as Anatolia and Iran reasonably well below 60 km. Because of the global ISC dataset, in Egypt and its surrounding regions, the resolution increases below ~ 800 km, especially of the large-scale features in the lower mantle.

The norm damping and smoothing parameters applied in the inversion are chosen based on the L-curve tests shown in Figs. S7-S12. We choose the model with a reduced chi-square misfit value of about 0.8, considering the standard data errors estimated for our regional data set, including the P-wave onset-time readings from waveforms. The selection of inversion parameters is made with consideration based on the resolution of the checkerboard tests with 4% P-velocity perturbations shown in Figs. 6 & 7. Although the $2.4^\circ \times 2.4^\circ$ checkerboard tests show reasonably good recovery of the checkers for $r = 1$ with 1% damping, considering the smearing and amplitude recovery, we select a model with a higher damping of 2% (see Fig. S10).

Considering the decrease in the resolution below $\sim 1,000$ km, we show the horizontal sections taken at various depths from 68 km down to 858 km inverted by the combined data set of the ISC data with onset-time readings from the waveform data in Fig. 8. Additional onset-time readings from waveforms improve the tomographic images, mainly within the lithosphere underneath the Arabian plate, compared to the inversion results obtained with the ISC data only (see Fig. S2 for comparison). We observe the sharp boundary between the Arabian shield and the Arabian platform down to about 300 km, taking advantage of the additional dataset from waveforms, which is not that clear from the inversion results with the ISC data only (Fig. S2). In the lithosphere, down to ~ 135 km, a low-velocity anomaly start-

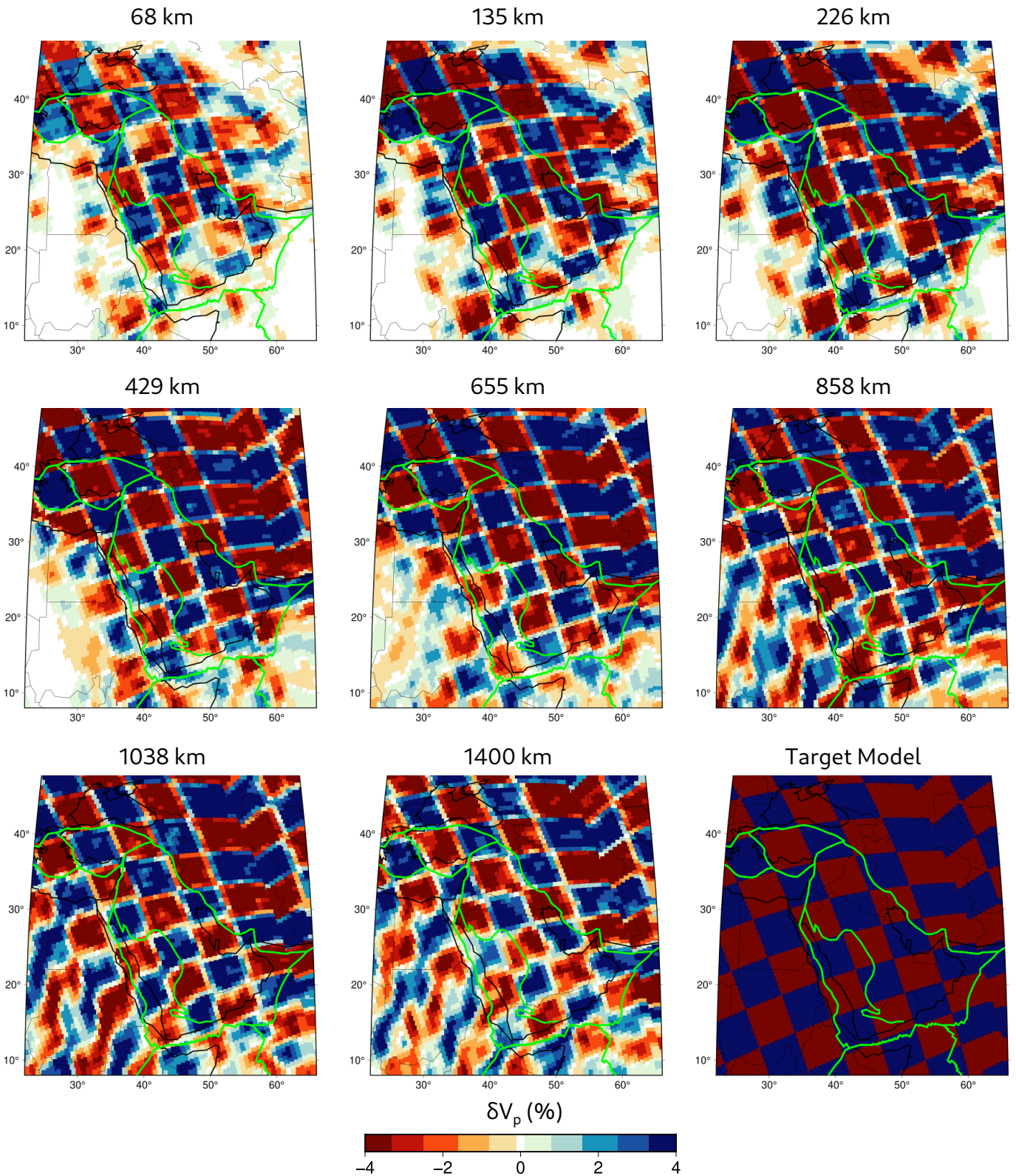


Figure 6 Horizontal cross-sections of the $4^\circ \times 4^\circ$ checkerboard test results for P-wavespeed perturbations at various depths with the ISC data and onset-time readings from waveform data recorded by the SGS stations.

ing from Afar extends northward to the Caucasus area, which is well correlated with volcanism along the Red Sea, in the Arabian shield and Eastern Anatolia. The low-velocity anomaly along the Red Sea is shifted to the East toward Harrats around 70 km, which is observed just below the Red Sea around 200-km depth (Fig. 8), consistent with previous models of the region (e.g., Kim et al., 2023). The resolution on the western part of the

Red Sea (i.e., Egypt) improves below ~ 500 km due to the global ISC data coverage.

We clearly observe the subduction along the Hellenic arc (Fig. 9, sections AA'-CC') with potential slab detachments in the upper and lower mantle, where the corresponding checkerboard tests show decent resolution power of data along the subduction (Fig. S5). The perturbations of the shallower Cyprus arc are less than

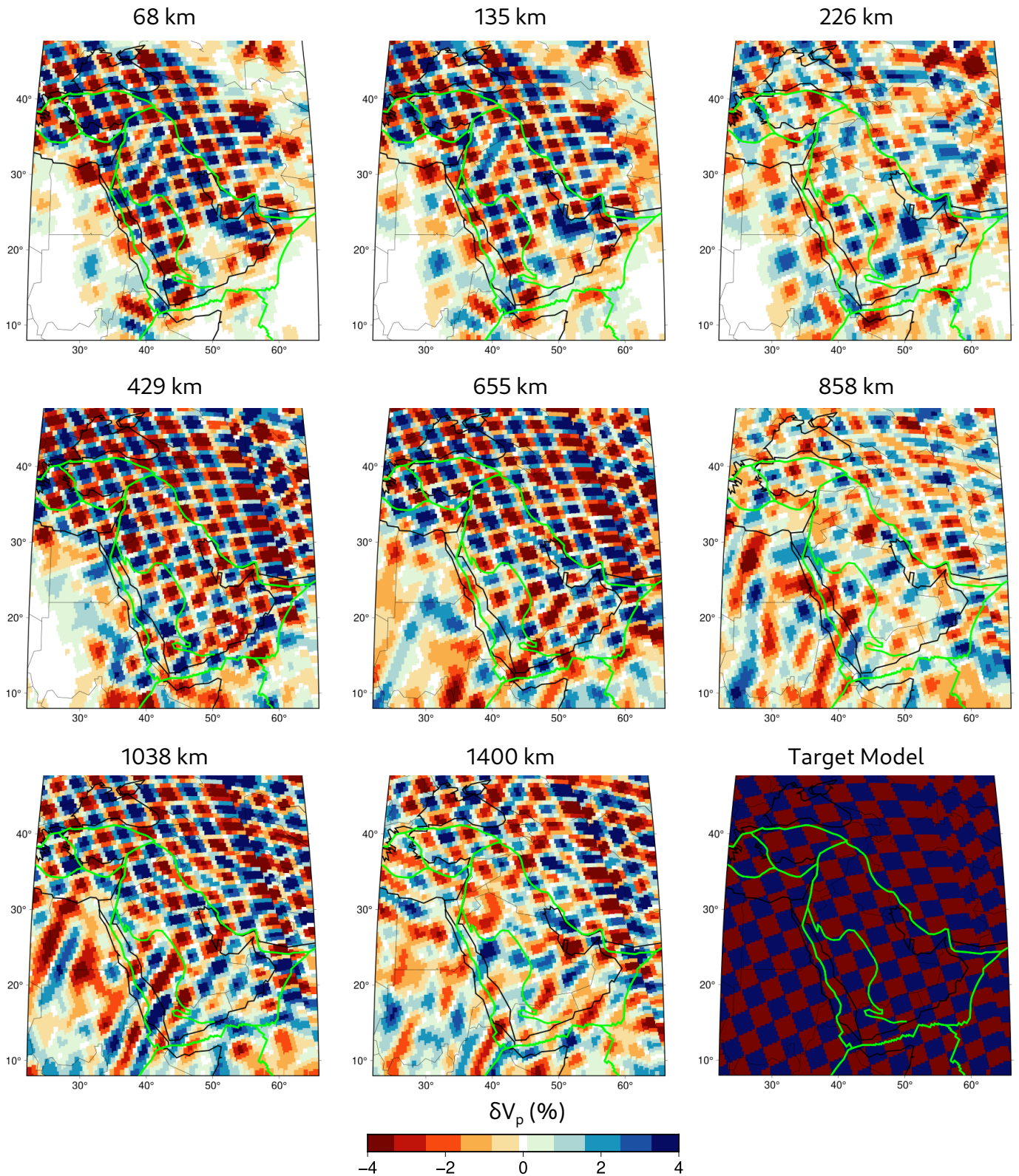


Figure 7 Same as Fig. 6 but for the $2.4^\circ \times 2.4^\circ$ checkerboard test results.

those of the Hellenic arc but clearly visible (Fig. 9, section CC'). The two low-velocity zones above 200 km depth along sections DD' and EE' are well correlated with the volcanic province Harrat al-Sham in Southern Syria and the volcanism in Eastern Anatolia and the Caucasus, respectively. The low velocities in the lithosphere underneath the Eastern and Central Anatolia are also clearly visible in section FF'. On the other hand, the potential remnant of the subduction along the Bitlis su-

ture zone is observed as high-wavespeed perturbations just above 660 km discontinuity underneath Anatolia (Fig. 9, section FF'). The checkerboard test results along the same paths and depth range show good recovery of checkers (Fig. S5).

The cross sections across the Zagros suture zone show evidence of the eastern edge of the Arabian plate lithosphere being underthrust beneath the western edge of the Eurasian plate at collision (Fig. 10, sec-

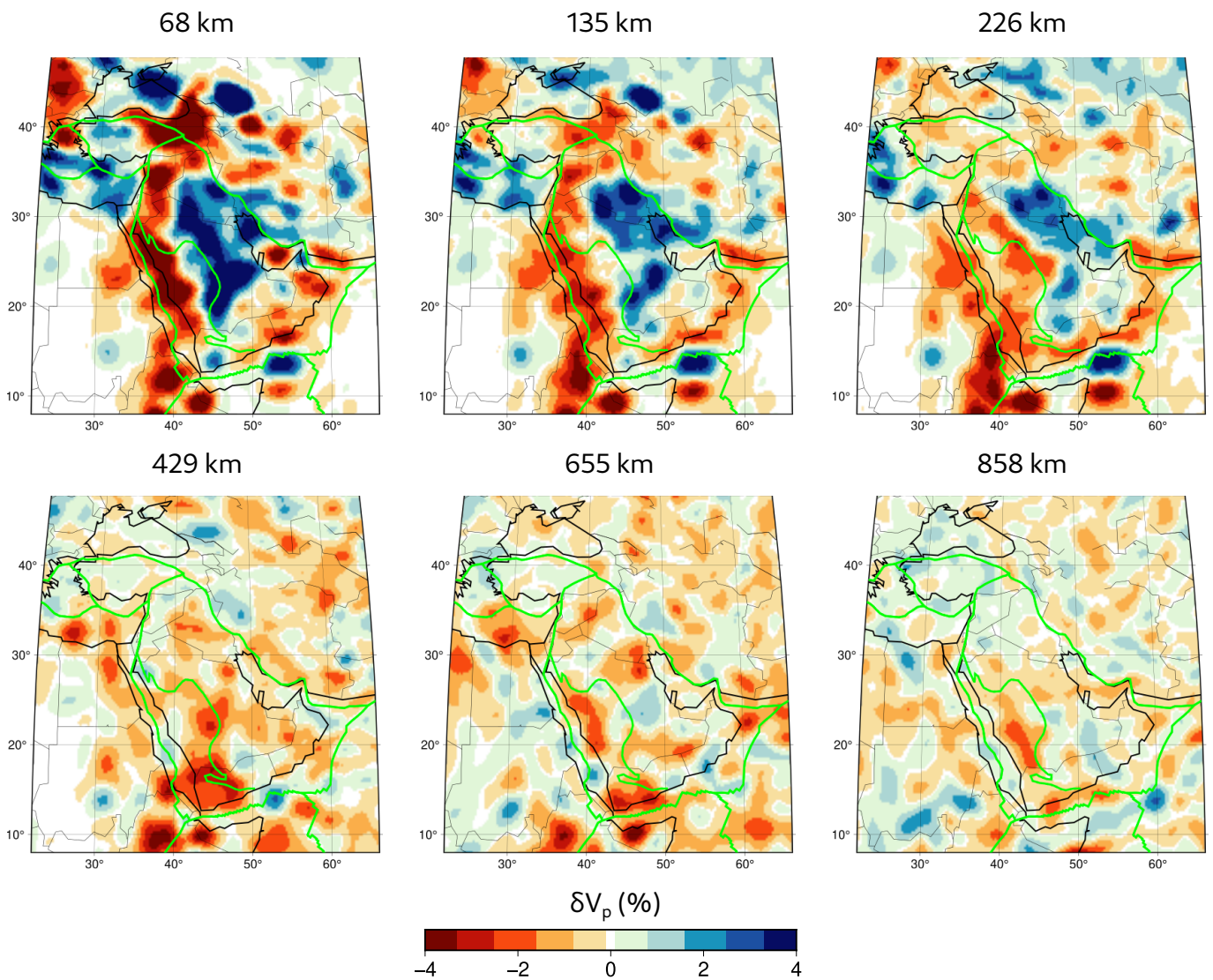


Figure 8 Horizontal cross-sections of P-wavespeed perturbations of the inverted model with respect to AK135 at various depths. ISC data combined with onset-time readings from waveforms recorded by the SGS stations are used during the inversion.

tions AA'-DD'). From sections AA'-DD', the subducted Tethys Ocean underneath Iran along the suture zone is visible down to 300 km. The subduction can be observed down to 660 km and penetrates the lower mantle with a steeper angle as we go toward the South. The checkerboard tests, in general, show good resolution along the Zagros suture zone and on the East down to about 600 km depth, supporting the observations. However, the resolution decreases towards the South in the Arabian plate, which is clearly seen in section DD' (Fig. S6). The western part of the sections from AA' to DD' highlights the Red Sea and volcanism under the Harrats and Yemen, with low-velocity perturbations in the upper mantle extending to the lower mantle where the decreased checkerboard resolutions are observed correlated to the data coverage. The cross-sections along the Red Sea and the Arabian shield from South to North (EE'-FF') depict the channeled low velocities within the top 300 km, which are deeper in the South and extend to the lower mantle. Section GG' shows similar low-velocities on the southern edge while high-wavespeed perturbations characterize the litho-

sphere of the Arabian platform toward the North, overlying the low-velocity zone below about 300 km. The low-velocity zone in the southern edge of profile HH' is well-correlated with the volcanism in the Makran region and the fore-arc volcanism due to subduction along the Zagros suture as well as the volcanic region in Eastern Anatolia and Caucasus, where we have good resolution. Although the checkerboard tests clearly show the degraded resolution on all sections on the west of the Red Sea and along sections CC' and DD', the long wavelength features are retrievable (Fig. S6).

In Fig. 11, we compare our model to the P-wave perturbations of Simmons et al. (2021), the S-wave perturbations of Chang and Van der Lee (2011) and the P-wave perturbations of Celli et al. (2020) in the upper mantle with respect to their mean models (see Fig. S14 for perturbations with respect to AK135). Both Simmons et al. (2021) and Celli et al. (2020) also have their S-wavespeed models, which can be seen in Fig. S15. Our P-wave perturbations are larger than those of the global model of Simmons et al. (2021), where the low-velocity regions are better resolved in our model below

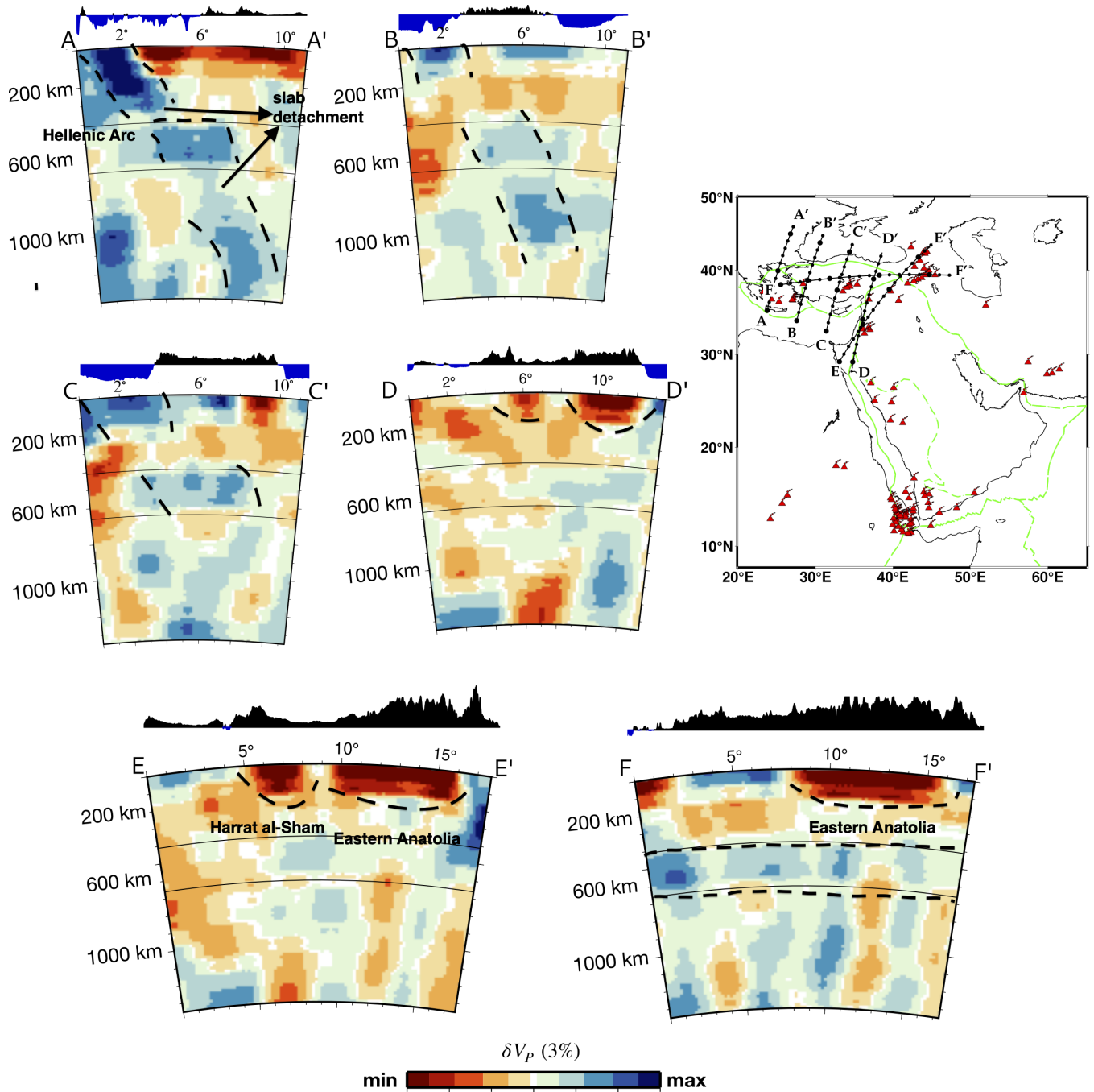


Figure 9 Same as Fig. 8 but for vertical sections traversing the Hellenic and Cyprus arcs and Anatolia.

about 150 km. P- and S-wavespeed models of Celli et al. (2020) show the long-wavelength structure of our study region as a result of their construction as part of the African continent tomography. Overall, the long wavelength structures of the P and S models are consistent. There is, in general, a good correlation between our P-wave model and Chang and Van der Lee (2011)’s S-wave model, where the main discrepancies in the Arabian Peninsula might be coming from different wavespeed models and the additional dataset we used in our inversions. We observe the largest discrepancy around 200 km. The strong northwest-southeast linear low-velocity trend in the Arabian Peninsula in the S-wave model of Chang and Van der Lee (2011), and the following P-wave model from the same group (Chang et al., 2012) around 200 km is less pronounced in our model

where we can still clearly track the boundary between the Arabian shield and platform down to at least 300 km (see Fig. S16). The northwest-southeast linear trend is slightly observed in our model below 350 km. Our P-wave model is more in agreement with the Chang and Van der Lee (2011)’s model at around 450-500 km. We also compare our model to the vertical cross-sections presented in Chang and Van der Lee (2011) along three profiles in Fig. 12. The largest discrepancy is on the African side of section AA’, where our model has limited resolution in the upper mantle (see Figs. 7 & S17). The low- and fast-wavespeed anomalies in the upper mantle along section BB’ overall agree with each other, where we have a decent resolution (Fig. S17), while the high-wavespeed anomaly in the Arabian platform is wider and deeper. The two potential mantle plumes suggested

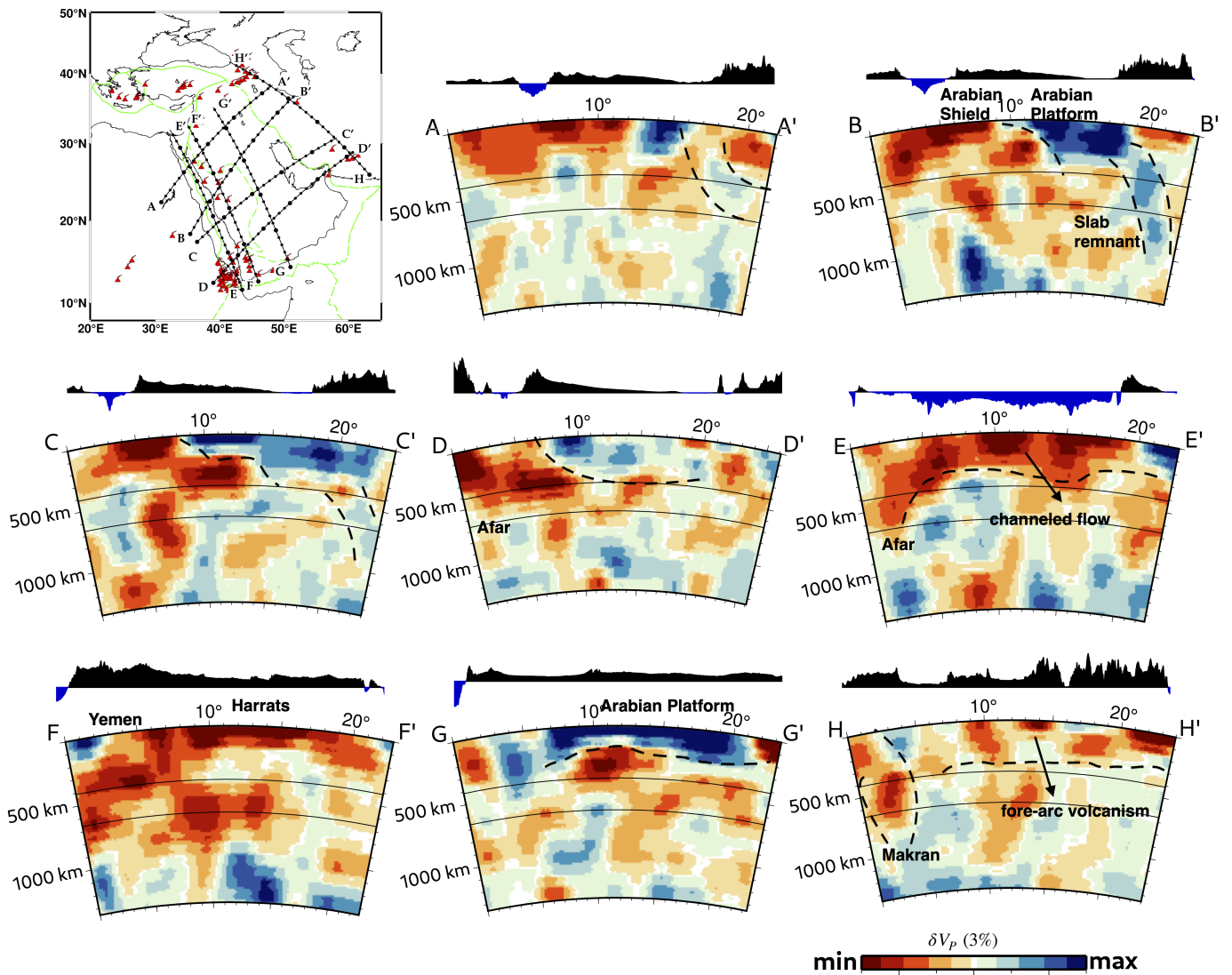


Figure 10 Same as Fig. 9 but for vertical sections traversing the Arabian shield, Arabian platform, Persian Gulf and Zagros suture zone.

by Chang and Van der Lee (2011) along the same profile are also present in our model but are less tractable in the lower mantle. Both models capture the subduction along Zagros (section CC') together with the low-wavespeed anomalies surrounding it, which likely extend to the lower mantle. However, the shape and depth extension of the subduction need further investigation.

4 Discussions

Our P-wave model, MEPT, shows the distinct separation of the Arabian platform and the Arabian shield, characterized by high- and low-wavespeed perturbations, respectively, in the upper mantle down to about 300 km (Fig. 8). The Arabian platform and the shield expose themselves clearly in the surface geology (Fig 1). The boundary between these two tectonic units has also been reported in previous studies. For instance, Chang and Van der Lee (2011) observe it below 75 km based on their S-wavespeed model of the region where the sharp discontinuity also presents in Lim et al. (2020)'s S-wave model based on the arrival times of S and SKS phases plotted starting at 100 km depth. The P and S-wave mod-

els constructed based on surface waves by Kim et al. (2023) and Celli et al. (2020)'s work as part of the larger African tomography also show this boundary clearly after about 70 km. In our model, the boundary between these two tectonic units is more pronounced and well-identified, from 100 km down to at least 300 km where we have good data coverage with the additional arrival-time picks (see Figs. 3 & 5). Kaviani et al. (2020) also observes this boundary around 90 km based on their ambient-noise study in the same region but again with lower resolution. Although it is not visible in our model directly, which is an upper mantle model with limited resolution in the crust, based on the crustal models of the region, the wavespeed perturbations seem to be reversed from the crust to the mantle where the Arabian platform is characterized by low-wavespeed perturbations in the crust due to the sedimentary basins (i.e., Mesopotamian Basin), and the Arabian shield is characterized by relatively higher perturbations (e.g., Bassin et al., 2000; Kaviani et al., 2020). The clear separation between the Arabian platform and the shield in the crust and the upper mantle with the velocity reversal is also consistent with a recent study of the crustal and man-

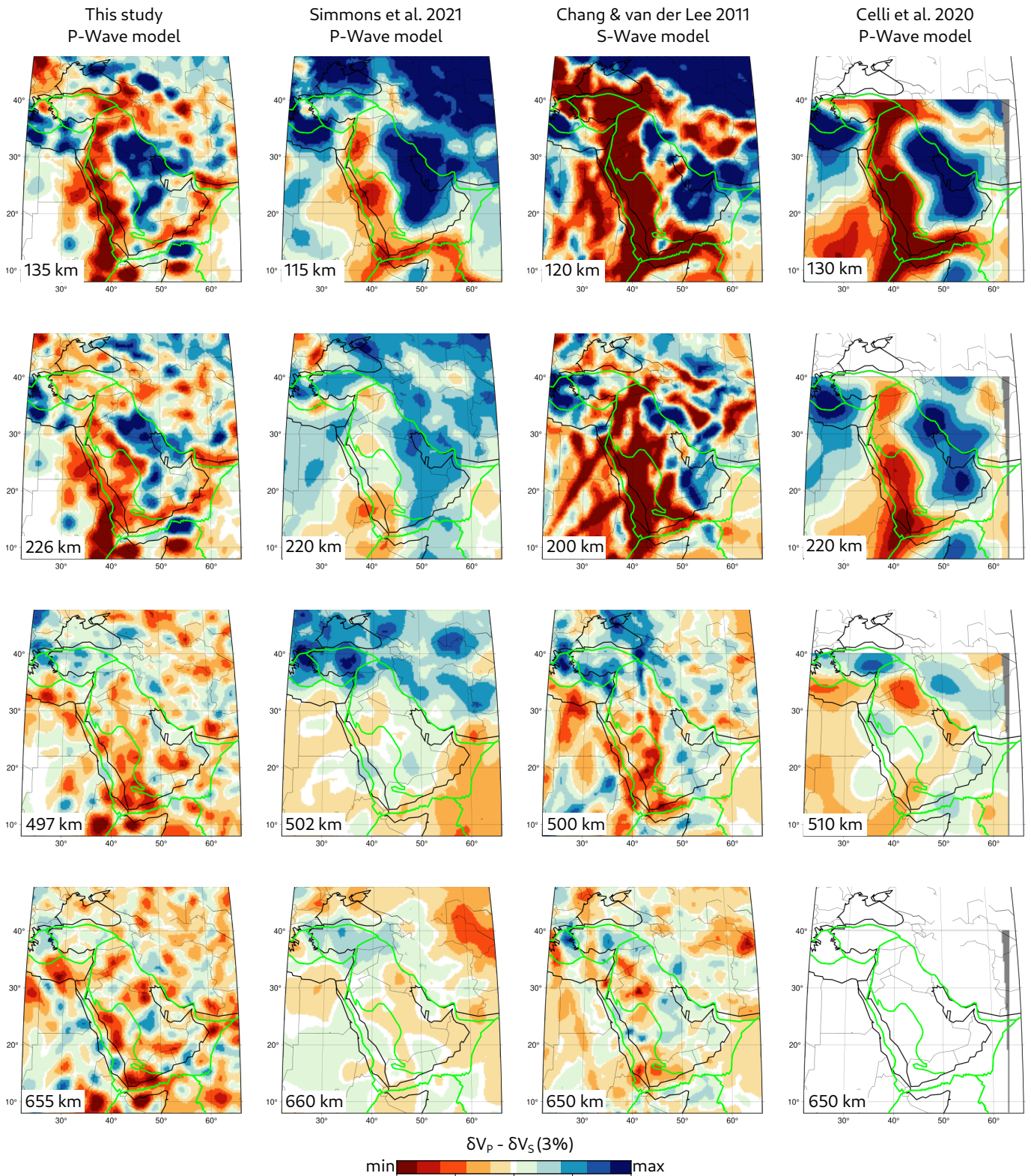


Figure 11 Comparison of the horizontal sections of the P-wavespeed model of Simmons et al. (2021), the S-wavespeed model of Chang and Van der Lee (2011), and the P-wavespeed model of Celli et al. (2020) to the P-wavespeed model from this study. Perturbations are plotted with respect to the mean of each model. See Fig. S14 & S15 for comparisons of P- and S-wavespeed cross-sections plotted with respect to AK135.

the attenuation structure of the region based on Lg-wave observations and measurements where the lithosphere and upper mantle underneath the shield and the platform are characterized by low and high Q (quality factor, the inverse of attenuation) values down to ~ 180 and up to $\sim 5,600$, respectively (Pasyanos et al., 2021).

The relatively slower wavespeeds in the platform compared to the shield in the crust reported in (e.g., Kaviani et al., 2020) is also supported by the crustal Q model by Pasyanos et al. (2021) where the absence of Lg waves are observed. On the other hand, the faster P wavespeeds in the platform compared to those in the shield we ob-

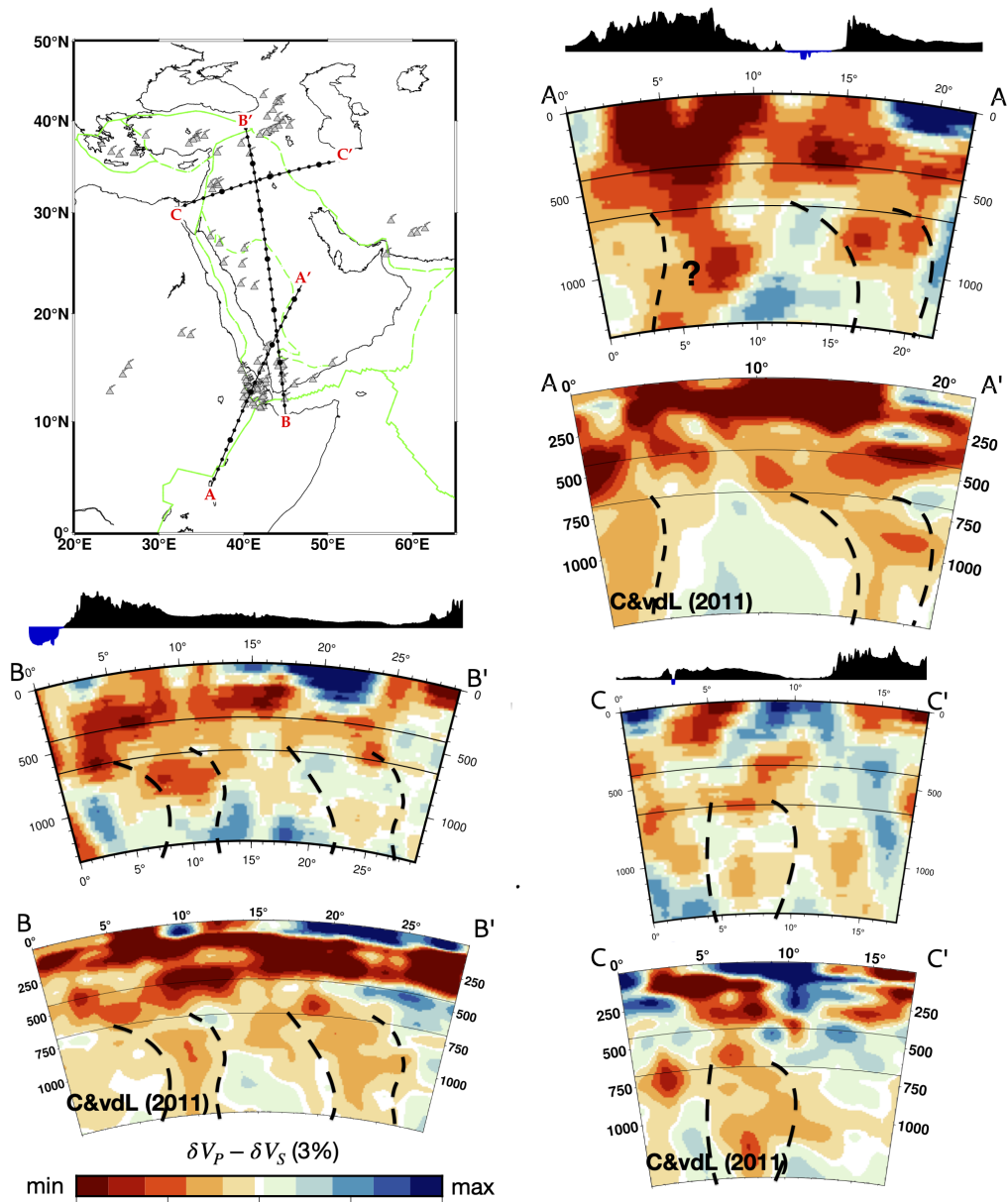


Figure 12 Comparison of the vertical sections of the S-wavespeed model of Chang and Van der Lee (2011) and the P-wavespeed model from this study. Perturbations are plotted with respect to AK135.

serve in the upper mantle might be partially because of the remnant of subduction along the Zagros collision zone. The slower P wavespeeds in the Arabian shield are likely related to the volcanism due to the proposed plume models in the Arabian plate as well as the rifting processes along the Red Sea (e.g., Koulakov et al., 2016; Pasyanos and Walter, 2002; Chang and Van der Lee, 2011).

There is no consensus on the origin of the volcanism of the Harrats, the largest continental alkali basalt province in Saudi Arabia extending from Yemen in the South to Syria, where there are records of historical eruptions close to major cities such as Medinah (e.g., Moufti and Németh, 2016). The low velocities observed along the Red Sea and Gulf of Aden are consistent with the continental rifting and spreading ridge. On the other hand, there is evidence for a channel of flow

northward to Eastern Anatolia originated from the Afar plume from geochemical data and seismic tomographic models (e.g., Ebinger and Sleep, 2011; Chang et al., 2012; Park et al., 2007) which is also supported by the SKS observations in the region (e.g., Park et al., 2008; Hansen et al., 2008). Our tomographic model does not rule out the theory of spreading-related volcanism in the region. However, the cross-sections along the Red Sea (see Fig. 10) suggest the potential channeled flow from Afar to Syria with deeper and higher perturbations closer to Afar in the South. A similar observation was also reported by Lim et al. (2020). Some global models show the potential connection of the Afar plume to the African superplume (e.g., Montelli et al., 2004; Ritsema et al., 2011; Lei et al., 2020) while some other studies propose regional plumes or mantle upwelling underneath the Arabian plate which may or may not be re-

lated to Afar or the African superplume in the broader scale (e.g., Chang et al., 2012; Koulakov et al., 2016). A recent study by Kim et al. (2023) discusses that their model does not support a local plume underneath the Arabian plate and cannot resolve the Jordan plume reported by Chang and Van der Lee (2011) and Koulakov et al. (2016). Our P-wave model seems to be resolving the mantle upwellings underneath the Arabian platform and Jordan, supporting the observations of Chang and Van der Lee (2011) (Fig. 12, also see vertical resolution in Fig. S17). In addition, the northeast extension of the channeled low-velocity anomaly in the Arabian Peninsula observed in Chang and Van der Lee (2011) at 200 km (Fig. 11) is observed in our model slightly at a much deeper depth, after 350 km (Figs 11 & S14), which is likely another support for the local plumes by our model.

Although the data coverage in the south of the Hellenic arc is not sufficient, the areas north of the Hellenic arc are well resolved (Figs. 5, 7) due to better station coverage in Anatolia. The fast P-wave speed anomalies are related to the Hellenic-Cyprus arcs (Fig. 9), and we observe a potential slab detachment beneath 200 km (see sections BB'-CC' in Fig. 9 and corresponding checkerboard tests in Fig. S5). Similar observations were also made in previous regional tomographic images produced by surface waves (e.g., Meier et al., 2007), P-wave arrival times (e.g., Spakman et al., 1988; Wei et al., 2019) as well as the adjoint tomography models (e.g. Zhu et al., 2012). We also observe a further weakening in the lower mantle. The Hellenic slab becomes stagnant above 660 km before penetrating the lower mantle and appears to reach a 1,000 km depth. This stagnation was also reported previously (Biryol et al., 2011; Piromallo and Morelli, 2003; Portner et al., 2018; Wortel and Spakman, 2003), likely the remnant of the subducted and detached Tethys Ocean, which can be tracked on an East-West section across Anatolia (Fig. 9). As we move further East, at the western side of the Cyprus arc, we observe a dipping fast anomaly that disappears around 200 – 300 km, a possible tear in the slab filled with hot material followed by fast material on top of 660 km (Fig. 9B). The fast anomaly observed on top of the 660 km discontinuity is the remnant of the subduction of the Tethys Ocean underneath Anatolia (e.g., Biryol et al., 2011; Abgarmi et al., 2017). The Aegean basin and Eastern Anatolia are characterized by slow wavespeeds correlated well with subduction-related volcanism. The attenuation of Sn waves was also previously attributed to the absence of the lithospheric mantle below in Eastern and central Anatolia and the Iranian Plateau by Gök et al. (2003). The pronounced slow P wavespeeds we observe underneath Eastern Anatolia and along the Zagros fold may be correlated with high attenuation in these regions characterized by the absence of Sn waves and can indicate partial melting associated with the subduction and volcanism in the area.

We clearly observe fast-wavespeed perturbations along the Bitlis suture zone in the upper mantle where the remnant of the Tethys Ocean lies over the 660 km discontinuity underneath Eastern Anatolia which was also shown by the models of (e.g., Biryol et al., 2011;

Zhu et al., 2012). Similar anomalies along the Zagros suture zone (Fig. 10) are also observed in this and previous studies underneath the Iranian plateau (e.g., Simmons et al., 2012; Pasyanos and Walter, 2002; Shapiro and Ritzwoller, 2002; Debayle and Sambridge, 2004; Lebedev and van der Hilst, 2008) associated with the collision. The collision models of the Zagros suture also discuss the possibility of double subduction models related to the rifting history of the Neo-Tethys Ocean (e.g., Jafari et al., 2023). Although the observed fast-wavespeed anomalies in the mantle east of Zagros may be considered for discussions of the potential double subduction, further investigation is needed.

Seismic source studies require more accurate crustal and upper-mantle models of both P and S wavespeeds. P-wavespeed models are more challenging to be constructed mainly because of the relatively poor data coverage compared to S-wavespeed models, which can generally be combined with surface waves. Further improvements in tomographic models cannot be achieved without better spatial sampling. With the additional data from the Arabian Peninsula, we observe significant improvement in the resolution of the P-wave structure underneath the Middle East. We note that the resolution enhancement caused by onset-time readings from waveforms in this study is restricted to the upper mantle depths because we used regional events only in our arrival-time tomography. The resolution in deeper parts can be further improved by using waveforms from teleseismic events. In addition, our resolution in the crust is limited, which is fixed to Crust2.0 (Bassin et al., 2000) during the inversion. We expect that a higher resolution crustal model such as Crust1.0 (Laske et al., 2012), the successor of Crust2.0, should not change our overall conclusions. However, the effect of crust on seismic waves is well known, not only on surface waves (e.g., Bozdağ and Trampert, 2008; Ferreira et al., 2010) but also on body waves (Ritsema et al., 2002), which may have an impact on our inference particularly on upper-mantle anisotropy. To minimize leakage from the crust to the upper mantle, Moho perturbations have been inverted as a parameter in some studies. (e.g., van der Lee and Nolet, 1997; Witek et al., 2023). The simultaneous inversion of the crustal and upper mantle structure is desirable, which is the subject of a future publication within a full-waveform inversion framework. On the other hand, the resolution of the P-wavespeed models is still largely controlled by their limited data coverage compared to that of S waves. Cui et al. (2024) recently tackled this issue by balancing P- and S-wave contributions through appropriate weighting schemes in an adjoint tomography framework. Combining arrival times with waveforms can be another way to enhance, specifically P-wave models. Our goal is to demonstrate combining arrival-time data or models in the adjoint inversion of the region. Such an approach may also have the potential to expand the study to the oceanic areas sampled with emerging acoustic instruments such as MERMAIDS (Sukhovich et al., 2015) where the onset-time readings from MERMAID data may potentially be assimilated in adjoint inversions in a similar way.

We also note that the recovery of amplitudes in

checkerboard tests is not perfect, which is a common problem for traveltimes tomographic studies for several reasons, such as data coverage, damping used in the inverse problem, etc. To further improve the resolution of the tomographic models of the region, full-waveform inversion (e.g., Tarantola, 1984; Tape et al., 2009; Fichtner et al., 2010; Zhu et al., 2012) is the way forward, potentially with also carefully assimilating amplitudes of waveforms in inversions. However, although the inclusion of the amplitude information is desirable to constrain the heterogeneities better (e.g., Laske and Masters, 1996) as they are sensitive to the gradient of phase speeds (Woodhouse and Wong, 1986), the trade-off between wavespeeds, attenuation, and source uncertainties makes the inversions more challenging (e.g., Espindola-Carmona et al., 2024).

5 Conclusions

We present a higher-resolution P-wavespeed model, MEPT, of the Middle East and the surrounding region constructed based on teleseismic and regional arrival times of the first-arrival P waves collected from the most recently reinterpreted ISC-EHB bulletin (Engdahl et al., 2020) and onset-time readings from waveforms recorded by the Saudi Geological Survey (SGS) network on the Arabian Peninsula. The main strength of our model is the additional onset-time readings from regional waveforms, which significantly improves the lithospheric and upper mantle structure, specifically underneath the Arabian Peninsula.

Our model shows evidence of channeled flow northward from the Afar plume and supports the model of smaller mantle upwellings underneath the Arabian plate and Jordan to explain the origin of the volcanic fields in the region. The combined arrival times sharpen the boundary between the Arabian shield and the Arabian platform in the upper mantle, which is clearly observed at least down to 300-km depth. We also observe clear evidence of subduction along the Hellenic and Cyprus arcs with potential slab detachments, as well as the imprint of the collision along the Bitlis-Zagros suture zone following the closure of the Tethys Ocean. The observed slow P-wave anomalies in Eastern Anatolia and along the Zagros fold are likely related to the absence of the lithospheric mantle, which was previously interpreted by the attenuation of Sn waves.

In future studies, our goal is to assimilate the waveforms from the SGS network in an adjoint tomography setup to further improve the resolution through the simultaneous inversion of the crust and upper mantle for geological and tectonic interpretations as well as providing 3D reference models for source location and characterization studies. Ultimately, a framework that combines all available data (i.e., including arrival times in full-waveform inversion workflows) would be beneficial to improve the resolution of P-wavespeed models, which could potentially be extended to oceanic domains as well.

Acknowledgements

The authors thank Editor Suzan van der Lee and two reviewers for their constructive comments and careful reviews, which improved the earlier versions of the manuscript. This study was supported by the Air Force Research Laboratory project with grant number FA9453-19-C-0068 and the National Science Foundation with grant numbers EAR-1945565 and OAC-2103621. The authors gratefully acknowledge the arrival-time data from the International Seismological Centre (ISC)-EHB Bulletin (<http://www.isc.ac.uk/isc-ehb/>), and waveform data from the Saudi Geological Survey.

Data and code availability

The traveltimes inversion software BD-soft is available from

<https://www.geoazur.fr/GLOBALSEIS/Soft.html>.

The P-wave model, MEPT, constructed in this study is available from Zenodo

<https://doi.org/10.5281/zenodo.15115349>.

The P-wave arrival-time data is freely available from the International Seismological Centre (ISC)-EHB Bulletin (<http://www.isc.ac.uk/isc-ehb/>). The waveform data used in this study is not open-access, which is maintained and provided by the Saudi Geological Survey.

Competing interests

Authors have no competing interests.

References

- Abgarmi, B., Delph, J. R., Ozacar, A. A., Beck, S. L., Zandt, G., Sandvol, E., Turkelli, N., and Biryol, C. B. Structure of the crust and African slab beneath the central Anatolian plateau from receiver functions: New insights on isostatic compensation and slab dynamics. *Geosphere*, 13(6):1774–1787, 2017. doi: 10.1130/GES01509.1.
- Adams, A., Brazier, R., Nyblade, A., Rodgers, A., and Al-Amri, A. Source parameters for moderate earthquakes in the Zagros Mountains with implications for the depth extent of seismicity. *Bull. Seismol. Soc. Am.*, 99(3):2044–2049, 2009. doi: 10.1785/0120080314.
- Agard, P., Omrani, J., Jolivet, L., and Mouthereau, F. Convergence history across Zagros (Iran): constraints from collisional and earlier deformation. *International Journal of Earth Sciences*, 94(3):401–419, 2005. doi: 10.1007/s00531-005-0481-4.
- Al-Damegh, K., Sandvol, E., Al-Lazki, A., and Barazang, M. Regional seismic wave propagation (Lg and Sn) and Pn attenuation in the Arabian Plate and surrounding regions. *Geophys. J. Int.*, 157(2): 775–795, 2004. doi: 10.1111/j.1365-246X.2004.02246.x.
- Al-Lazki, A., Sandvol, E., Buland, Seber, D., Barazangi, M., Turkelli, N., and Mohamad, R. Pn tomographic imaging of mantle lid velocity and anisotropy at the junction of the Arabian, Eurasian and African plates. *Geophys. J. Int.*, 158:1024–1040, 2004. doi: 10.1111/j.1365-246X.2004.02355.x.
- Almalki, K. A., Betts, P. G., and Ailleres, L. The Red Sea – 50-year-geological and geophysical research. *Earth-Sci. Rev.*, 147: 109–140, 2015. doi: 10.1016/j.earscirev.2015.05.002.

- Artemieva, I., Yang, H., and Thybo, H. Incipient Ocean spreading beneath the Arabian shield. *Earth-Sci. Rev.*, 226:103955, 2022. doi: 10.1016/j.earscirev.2022.103955.
- Augustin, N., van der Zwan, F., Devey, C., and Brandsdóttir, B. 13 million years of seafloor spreading throughout the Red Sea Basin. *Nat. Commun.*, 12:2427, 2021. doi: 10.1038/s41467-021-22586-2.
- Ball, P., Roberts, G., Mark, D., Barfod, D., White, N., Lodhia, B., Nahdi, M., and Garni, S. Geochemical and geochronological analysis of Harrat Rahat, Saudi Arabia: An example of plume related intraplate magmatism. *Lithos*, 446-447:107112, 2023. doi: 10.1016/j.lithos.2023.107112.
- Bassin, C., Laske, G., and Masters, G. The current limits of resolution for surface wave tomography in North America. *EOS*, 81, 2000.
- Bijwaard, H., Spakman, W., and Engdahl, E. R. Closing the gap between regional and global travel time tomography. *Journal of Geophysical Research: Solid Earth*, 103(B12):30055–30078, 1998. doi: 10.1029/98JB02467.
- Bird, P. An updated digital model of plate boundaries. *Geochemistry, Geophysics, Geosystems*, 4(3), 2003. doi: 10.1029/2001GC000252.
- Biryol, C., Beck, S. L., Zandt, G., and Ozacar, A. Segmented African lithosphere beneath the Anatolian region inferred from teleseismic P-wave tomography. *Geophys. J. Int.*, 184:1037–1057, 2011. doi: 10.1111/j.1365-246X.2010.04910.x.
- Bonatti, E. Punctiform initiation of seafloor spreading in the Red Sea during transition from a continental to an oceanic rift. *Nature*, 316:33–37, 1985. doi: 10.1038/316033a0.
- Bozdağ, E. and Trampert, J. On Crustal Corrections in Surface Wave Tomography. *Geophysical Journal International*, 172(3): 1066–1082, Mar. 2008. doi: 10.1111/j.1365-246X.2007.03690.x.
- Bozdağ, E., Peter, D., Lefebvre, M., Komatitsch, D., Tromp, J., Hill, J., Podhorszki, N., and Pugmire, D. Global adjoint tomography: first-generation model. *Geophys. J. Int.*, 207(3):1736–1766, 2016. doi: 10.1093/gji/ggw356.
- Bozkurt, E. Neotectonics of Turkey—a synthesis. *Geodinamica Acta*, 14(1-3):3–30, 2001. doi: 10.1080/09853111.2001.11432432.
- Braunmiller, J. and Nábělek, J. Geometry of continental normal faults: seismological constraints. *Journal of Geophysical Research: Solid Earth*, 101(B2):3045–3052, 1996. doi: 10.1029/95JB02882.
- Braunmiller, J., Kradolfer, U., Baer, M., and Giardini, D. Regional moment tensor determination in the European–Mediterranean area—initial results. *Tectonophysics*, 356(1-3):5–22, 2002. doi: 10.1016/S0040-1951(02)00374-8.
- Camp, V. and Roobol, M. Upwelling asthenosphere beneath Western Arabia and its regional implications. *J. Geophys. Res.*, 97: 15255–15271, 2006. doi: 10.1029/92JB00943.
- Camp, V. E., Hooper, P. R., Roobol, M. J., and White, D. The Madinah eruption, Saudi Arabia: magma mixing and simultaneous extrusion of three basaltic chemical types. *Bulletin of Volcanology*, 49 (2):489–508, 1987. doi: 10.1007/BF01245475.
- Celli, N., Lebedev, S., Schaeffer, A., and Gaina, C. African cratonic lithosphere carved by mantle plumes. *Nat. Commun.*, 11:92, 2020. doi: 10.1038/s41467-019-13871-2.
- Chang, S.-J. and Van der Lee, S. V. Mantle plumes and associated flow beneath Arabia and East Africa. *Earth and Planetary Science Letters*, 302(3):448–454, 2011. doi: 10.1016/j.epsl.2010.12.050.
- Chang, S.-J., Van der Lee, S., and Flanagan, M. P. A new P-velocity model for the Tethyan margin from a scaled S-velocity model and the inversion of P- and PKP-delay times. *Physics of the Earth and Planetary Interiors*, 210-211:1–7, 2012. doi: 10.1016/j.pepi.2012.08.005.
- Charley, J., Voronin, S., Nolet, G., Loris, I., Simons, F. J., Sigloch, K., and Daubechies, I. C. Global seismic tomography with sparsity constraints: Comparison with smoothing and damping regularization. *Journal of Geophysical Research: Solid Earth*, 118(9): 4887–4899, 2013. doi: 10.1002/jgrb.50326, 2013.
- Chiang, A., Gök, R., Tarabulsi, Y. M., El-Hadidy, S. Y., Wael W. Rad-dadi, W. W., and Mousa, A. D. Seismic source characterization of the Arabian Peninsula and Zagros Mountains from regional moment tensor and coda envelopes. *Arabian Journal of Geosciences*, 14(9), 2021. doi: 10.1007/s12517-020-06266-x.
- Civilini, F., Mooney, W. D., Savage, M. K., Townend, J., and Zahran, H. Crustal imaging of northern Harrat Rahat, Saudi Arabia, from ambient noise tomography. *Geophys. J. Int.*, 219(3):1532–1549, 2019. doi: 10.1093/gji/ggz380.
- Coleman, R. G. and McGuire, A. V. Magma systems related to the Red Sea opening. *Tectonophysics*, 150(1):77–100, 1988. doi: 10.1016/0040-1951(88)90296-X.
- Cui, C., Lei, W., Liu, Q., Peter, D., Bozdağ, E., Tromp, J., Hill, J., Podhorszki, N., and Pugmire, D. GLAD-M35: a joint P and S global tomographic model with uncertainty quantification. *Geophys. J. Int.*, 239(1):478–502, 08 2024. doi: 10.1093/gji/ggae270.
- Debayle, E. and Sambridge, M. Inversion of massive surface wave data sets: Model construction and resolution assessment. *J. Geophys. Res.*, 109, 2004. doi: 10.1029/2003jb002652.
- Delaunay, A., Baby, G., Paredes, E. G., Fedorik, J., and Afifi, A. M. Evolution of the Eastern Red Sea Rifted margin: morphology, uplift processes and source-to-sink dynamics. *Earth-Science Reviews*, 250:104698, 2024. doi: https://doi.org/10.1016/j.earscirev.2024.104698.
- Duncan, R. A., Kent, A. J., Thornber, C. R., Schlieder, T. D., and Al-Amri, A. M. Timing and composition of continental volcanism at Harrat Hutaymah, western Saudi Arabia. *Journal of Volcanology and Geothermal Research*, 313:1–14, 2016. doi: https://doi.org/10.1016/j.jvolgeores.2016.01.010.
- Ebinger, C. and Sleep, N. Cenozoic magmatism throughout east Africa resulting from impact of a single plume. *Nature*, 395: 788–791, 2011. doi: https://doi.org/10.1038/27417.
- Engdahl, E., Giacomo, D. D., Sakarya, B., Gkarlaoui, C., Harris, J., J., and Storchak, D. ISC EHB1964–2016, an improved data set for studies of Earth structure and globaleismicity. *Earth and Space Sci.*, 7:e2019EA000897, 2020. doi: 10.1029/2019EA000897.
- Engdahl, E. R., Jackson, J. A., Myers, S. C., Bergman, E. A., and Priestley, K. Relocation and assessment of seismicity in the Iran region. *Geophysical Journal International*, 167(2):761–778, 2006. doi: 10.1111/j.1365-246x.2006.03127.x.
- Espindola-Carmona, A., Orsvuran, R., Mai, P., Bozdağ, E., and Peter, D. B. Geophysical Journal International. *Earth and Planetary Science Letters*, 236(2):952–966, 2024. doi: 10.1093/gji/ggad462.
- Ferreira, A. M. G., Woodhouse, J. H., Visser, K., and Trampert, J. On the Robustness of Global Radially Anisotropic Surface Wave Tomography. *Journal of Geophysical Research: Solid Earth*, 115 (B4), 2010. doi: 10.1029/2009JB006716.
- Fichtner, A., Kennett, B. L. N., Igel, H., and Bunge, H.-P. Full waveform tomography for radially anisotropic structure: New insights into present and past states of the Australasian upper mantle. *Earth and Planetary Science Letters*, 290:270–280, 2010. doi: 10.1016/j.epsl.2009.12.003.
- Giardini, D., Basham, P., and Berry, M. The ILP's global seismic hazard assessment program for the UN/IDNDR. In *Natural disasters: protecting vulnerable communities: Proceedings of the Conference held in London, 13-15 October 1993*, pages 225–237.

- Thomas Telford Publishing, 1993. doi: 10.1029/91eo00383.
- Giardini, D., Danciu, L., Erdik, M., Şeşetyan, K., Tümsa, M. B. D., Akkar, S., Gülen, L., and Zare, M. Seismic hazard map of the Middle East. *Bulletin of earthquake engineering*, 16(8):3567–3570, 2018. doi: 10.1007/s10518-018-0347-3.
- Gök, R., Kaviani, A., Matzel, E. M., Pasyanos, M. E., Mayeda, K., Yertirmishli, G., El-Hussain, I., Al-Amri, A., Al-Jeri, F., Godoladze, T., et al. Moment magnitudes of local/regional events from 1D coda calibrations in the broader Middle East region. *Bull. Seismol. Soc. Am.*, 106(5):1926–1938, 2016. doi: 10.1785/0120160045.
- Gök, R., Sandvol, E., Türkelli, N., Seber, D., and Barazangi, M. Sn attenuation in the Anatolian and Iranian plateau and surrounding regions. *Geophys. Res. Lett.*, 30(24):8042, 2003. doi: 10.1029/2003GL018020.
- Gök, R., Pasyanos, M. E., and Zor, E. Lithospheric structure of the continent-continent collision zone: eastern Turkey. *Geophys. J. Int.*, 169(3):1079–1088, 2007. doi: 10.1111/j.1365-246x.2006.03288.x.
- Hansen, S. E., Rodgers, A. J., Schwartz, S. Y., and Al-Amri, A. M. Imaging ruptured lithosphere beneath the Red Sea and Arabian Peninsula. *Earth and Planetary Science Letters*, 259(3-4): 256–265, 2007. doi: 10.1016/j.epsl.2007.04.035.
- Hansen, S. E., Gaherty, J. B., Schwartz, S. Y., Rodgers, A. J., and Al-Amri, A. M. Seismic velocity structure and depth-dependence of anisotropy in the Red Sea and Arabian shield from surface wave analysis. *Journal of Geophysical Research: Solid Earth*, 113(B10), 2008. doi: 10.1029/2007jb005335.
- Hatzfeld, D. and Molnar, P. Comparisons of the kinematics and deep structures of the Zagros and Himalaya and of the Iranian and Tibetan plateaus and geodynamic implications. *Reviews of Geophysics*, 48(2), 2010. doi: 10.1029/2009rg000304.
- International Seismological Centre. ISC-EHB dataset, 2020.
- Jafari, A., Ao, S., Jamei, S., and Ghasemi, H. Evolution of the Zagros sector of Neo-Tethys: Tectonic and magmatic events that shaped its rifting, seafloor spreading and subduction history. *Earth-Sci. Rev.*, 241:104419, 2023. doi: 10.1016/j.earscirev.2023.104419.
- Karasözen, E., Nissen, E., Bergman, E. A., Johnson, K. L., and Walters, R. J. Normal faulting in the Simav graben of western Turkey reassessed with calibrated earthquake relocations. *Journal of Geophysical Research: Solid Earth*, 121(6):4553–4574, 2016. doi: 10.1002/2016jb012828.
- Karasözen, E., Nissen, E., Bergman, E. A., and Ghods, A. Seismotectonics of the Zagros (Iran) from orogen-wide, calibrated earthquake relocations. *Journal of Geophysical Research: Solid Earth*, 124(8):9109–9129, 2019. doi: 10.1029/2019jb017336.
- Kaviani, A., Paul, A., Bourova, E., Hatzfeld, D., Pedersen, H., and Mokhtari, M. A strong seismic velocity contrast in the shallow mantle across the Zagros collision zone (Iran). *Geophysical Journal International*, 171(1):399–410, 2007. doi: 10.1111/j.1365-246x.2007.03535.x.
- Kaviani, A., Paul, A., Moradi, A., Mai, P. M., Pilia, S., Boschi, L., Rümpler, G., Lu, Y., Tang, Z., and Sandvol, E. Crustal and uppermost mantle shear wave velocity structure beneath the Middle East from surface wave tomography. *Geophysical Journal International*, 221(2):1349–1365, 2020. doi: 10.1093/gji/ggaa075.
- Kennett, B. L., Engdahl, E., and Buland, R. Constraints on seismic velocities in the Earth from traveltimes. *Geophysical Journal International*, 122(1):108–124, 1995. doi: 10.1111/j.1365-246x.1995.tb03540.x.
- Khrepy, S. E., Koulakov, I., Gerya, T., Al-Arifi, N., Alajmi, M., and Qadrouh, A. Transition from continental rifting to oceanic spreading in the northern Red Sea area. *Sci. Rep.*, 11:5594, 2021. doi: 10.1038/s41598-021-84952-w.
- Kim, R., Witek, M., Chang, S.-J., Lim, J.-A., Mai, P. M., and Zahran, H. Isotropic and radially anisotropic S-velocity structure beneath the Arabian plate inferred from surface wave tomography. *Tectonophysics*, 862:229968, 2023. doi: https://doi.org/10.1016/j.tecto.2023.229968.
- Kiuchi, R., Mooney, W. D., and Zahran, H. M. Ground-Motion Prediction Equations for Western Saudi Arabia. *Bull. Seismol. Soc. Am.*, 109(6):2722–2737, 2019. doi: 10.1785/0120180302.
- Koulakov, I., Burov, E., Cloetingh, S., El Khrepy, S., Al-Arifi, N., and Bushenkova, N. Evidence for anomalous mantle upwelling beneath the Arabian Platform from travel time tomography inversion. *Tectonophysics*, 667:176–188, 2016. doi: https://doi.org/10.1016/j.tecto.2015.11.022.
- Laske, G. and Masters, G. Constraints on global phase velocity maps from long-period polarization data. *Journal of Geophysical Research: Solid Earth*, 101(B7):16059–16075, 1996. doi: 10.1029/96jb00526.
- Laske, G., Masters, G., Ma, Z., and Pasyanos, M. Update on CRUST1.0 – A 1-degree Global Model of Earth's Crust. *EGU General Assembly Geophys. Res. Abstracts*, 15:EGU2012–3743–1, 2012.
- Le Pichon, X. and Kreemer, C. The Miocene-to-present kinematic evolution of the Eastern Mediterranean and Middle East and its implications for dynamics. *Annual Review of Earth and Planetary Sciences*, 38:323–351, 2010. doi: 10.1146/annurev-earth-040809-152419.
- Lebedev, S. and van der Hilst, R. D. Global upper-mantle tomography with the automated multimode inversion of surface and S wave forms. *Geophys. J. Int.*, 173:505–518, 2008. doi: 10.1111/j.1365-246x.2008.03721.x.
- Lei, W., Ruan, Y., Bozdağ, E., Peter, D., Lefebvre, M., Komatitsch, D., Tromp, J., Hill, J., Podhorszki, N., and Pugmire, D. Global Adjoint Tomography – Model GLAD-M25. *Geophys. J. Int.*, 223(1):1–21, 2020. doi: 10.1093/gji/ggaa253.
- Li, X.-D. and Romanowicz, B. Global mantle shear velocity model developed using nonlinear asymptotic coupling theory. *J. Geophys. Res.*, 101(B10):22245–22272, 1996. doi: 10.1029/96JB01306.
- Lim, J., Chang, S., Mai, P. M., and Zahran, H. Asthenospheric flow of plume material beneath Arabia inferred from S wave traveltime tomography. *Journal of Geophysical Research: Solid Earth*, 125:e2020JB019668, 2020. doi: https://doi.org/10.1029/2020JB019668.
- Maggi, A. and Priestley, K. Surface waveform tomography of the Turkish–Iranian plateau. *Geophysical Journal International*, 160(3):1068–1080, 2005. doi: 10.1111/j.1365-246x.2005.02505.x.
- McClusky, S., Balassanian, S., Barka, A., Demir, C., Ergintav, S., Georgiev, I., Gurkan, O., Hamburger, M., Hurst, K., Kahle, H., et al. Global Positioning System constraints on plate kinematics and dynamics in the eastern Mediterranean and Caucasus. *Journal of Geophysical Research: Solid Earth*, 105(B3):5695–5719, 2000. doi: 10.1029/1999jb900351.
- McKenzie, D. The structure of the lithosphere and upper mantle beneath the Eastern Mediterranean and Middle East. *Mediterranean Geoscience Reviews*, 2:311–326, 2020. doi: https://doi.org/10.1007/s42990-020-00038-1.
- Meier, T., Becker, D., Endrun, B., Rische, M., Bohnhoff, M., Stöckhert, B., and Harjes, H. A model for the Hellenic subduction zone in the area of Crete based on seismological investigations. *Geological Society, London, Special Publications*, 291:183–199, 2007. doi: 10.1144/sp291.9.

- Mokhtar, T. A. and Al-Saeed, M. M. Shear wave velocity structures of the Arabian Peninsula. *Tectonophysics*, 230(1-2):105–125, 1994. doi: 10.1016/0040-1951(94)90149-x.
- Montelli, R., Nolet, G., Masters, G., Dahlen, F., and Hung, S.-H. Global P and PP traveltime tomography: rays versus waves. *Geophys. J. Int.*, 158:637–654, 2004. doi: 10.1111/j.1365-246X.2004.02346.x.
- Moufti, M. R. and Németh, K. *Harrat Rahat: The Geoheritage Value of the Youngest Long-Lived Volcanic Field in the Kingdom of Saudi Arabia*, pages 33–120. Springer International Publishing, Cham, 2016. doi: 10.1007/978-3-319-33015-0_3.
- Mukhopadhyay, B., Mogren, S., Mukhopadhyay, M., and Dasgupta, S. Incipient status of dyke intrusion in top crust—evidences from the Al-Ays 2009 earthquake swarm, Harrat Lunayyir, SW Saudi Arabia. *Geomatics, Natural Hazards and Risk*, 4(1):30–48, 2013. doi: 10.1080/19475705.2012.663794.
- Nissen, E., Tatar, M., Jackson, J. A., and Allen, M. B. New views on earthquake faulting in the Zagros fold-and-thrust belt of Iran. *Geophysical Journal International*, 186(3):928–944, 2011. doi: 10.1111/j.1365-246x.2011.05119.x.
- Nissen, E., Jackson, J., Jahani, S., and Tatar, M. Zagros “phantom earthquakes” reassessed—The interplay of seismicity and deep salt flow in the Simply Folded Belt? *Journal of Geophysical Research: Solid Earth*, 119(4):3561–3583, 2014. doi: 10.1002/2013jb010796.
- Nolet, G. A breviary of seismic tomography. *A Breviary of Seismic Tomography*, by Guust Nolet, Cambridge, UK: Cambridge University Press, 2008. doi: 10.1017/cbo9780511984709.
- Nolet, G. and van der Lee, S. Error estimates for seismic body wave delay times in the ISC-EHB Bulletin. *Geophys. J. Int.*, 231: 1739–1749, 2022. doi: 10.1093/gji/ggac282.
- Nolet, G., Hello, Y., Van der Lee, S., Bonnieux, S., Ruiz, M. C., Pazmino, N. A., Deschamps, A., Regnier, M. M., Font, Y., Chen, Y. J., and Simons, F. J. Imaging the Galápagos mantle plume with an unconventional application of floating seismometers. *Scientific Reports*, 9:1326, 2019. doi: 10.1038/s41598-018-36835-w.
- Pallister, J. S., McCausland, W. A., Jónsson, S., Lu, Z., Zahran, H. M., El Hadidy, S., Aburukbah, A., Stewart, I. C., Lundgren, P. R., White, R. A., et al. Broad accommodation of rift-related extension recorded by dyke intrusion in Saudi Arabia. *Nature Geoscience*, 3(10):705–712, 2010. doi: 10.1038/ngeo966.
- Parisi, L., Augustin, N., Trippanera, D., Kirk, H., Dannowski, A., Matrau, R., Fittipaldi, M., Nobile, A., Zielke, O., Valero Cano, E., Hoogewerf, G., Aspiotis, T., Manzo-Vega, S., Espindola Carmona, A., Barreto, A., Juchem, M., Suhendi, C., Schmidt-Aursch, M., Mai, P. M., and Jónsson, S. The First Network of Ocean Bottom Seismometers in the Red Sea to Investigate the Zabargad Fracture Zone. *Seismica*, 3(1):104698, 2024. doi: <https://doi.org/10.26443/seismica.v3i1.729>.
- Park, Y., Nyblade, A., Rodgers, A., and Al-Amri, A. Upper mantle structure beneath the Arabian Peninsula and northern Red Sea from teleseismic body wave tomography: Implications for the origin of Cenozoic uplift and volcanism in the Arabian Shield. *Geochem. Geophys. Geosyst.*, 8:Q06021, 2007. doi: 10.1029/2006GC001566.
- Park, Y., Nyblade, A. A., Rodgers, A. J., and Al-Amri, A. S wave velocity structure of the Arabian Shield upper mantle from Rayleigh wave tomography. *Geochemistry, Geophysics, Geosystems*, 9(7), 2008. doi: 10.1029/2007gc001895.
- Pasyanos, M. E. and Walter, W. R. Crust and upper-mantle structure of North Africa, Europe and the Middle East from inversion of surface waves. *Geophysical Journal International*, 149:463–48, 2002. doi: 10.1046/j.1365-246x.2002.01663.x.
- Pasyanos, M. E., Walter, W. R., and Hazler, S. E. A surface wave dispersion study of the Middle East and North Africa for monitoring the Comprehensive Nuclear-Test-Ban Treaty. In *Monitoring the Comprehensive Nuclear-Test-Ban Treaty: Surface Waves*, pages 1445–1474. Springer, 2001. doi: 10.1007/978-3-0348-8264-4_7.
- Pasyanos, M. E., Tarabulsi, Y. M., Al-Hadidy, S. Y., Raddadi, W. W., Mousa, A. D., El-Hussain, I., Al-Jeri, F., Al-Shukri, H., and Gök, R. Improved lithospheric attenuation structure of the Arabian Peninsula through the use of national network data. *Arab J Geosci*, 14(914), 2021. doi: 10.1007/s12517-021-07294-x.
- Piromallo, C. and Morelli, A. P wave tomography of the mantle under the Alpine-Mediterranean area. *Journal of Geophysical Research*, 108:2065, 2003. doi: 10.1029/2002jb001757.
- Portner, D. E., Delph, J. R., Biryol, C. B., Beck, S. L., Zandt, G., and Qzacar, A. Subduction termination through progressive slab deformation across Eastern Mediterranean subduction zones from updated P-wave tomography beneath Anatolia. *Geosphere*, 14: 907–925, 2018. doi: 10.1130/ges01617.1.
- Reilinger, R. and McClusky, S. Nubia–Arabia–Eurasia plate motions and the dynamics of Mediterranean and Middle East tectonics. *Geophys. J. Int.*, 186:971–979, 2011. doi: 10.1111/j.1365-246X.2011.05133.x.
- Reilinger, R., McClusky, S., Vernant, P., Lawrence, S., Ergintav, S., Cakmak, R., Ozener, H., Kadirov, F., Guliev, I., Stepanyan, R., et al. GPS constraints on continental deformation in the Africa–Arabia–Eurasia continental collision zone and implications for the dynamics of plate interactions. *Journal of Geophysical Research: Solid Earth*, 111(B5), 2006. doi: 10.1029/2005jb004051.
- Ring, U., Glodny, J., Thomas Will, T., and Thomson, S. The Hellenic Subduction System: High-Pressure Metamorphism, Exhumation, Normal Faulting, and Large-Scale Extension. *Annu. Rev. Earth Planet. Sci.*, 38:45–76, 2010. doi: 10.1146/annurev.earth.050708.170910.
- Ritsema, J., Rivera, L. A., Komatitsch, D., Tromp, J., and van Heijst, H.-J. Effects of crust and mantle heterogeneity on PP/P and SS/S amplitude ratios. *Geophysical Research Letters*, 29(10): 72–1, 2002. doi: 10.1029/2001GL013831.
- Ritsema, J., Deuss, A., Van Heijst, H., and Woodhouse, J. S40RTS: a degree-40 shear-velocity model for the mantle from new Rayleigh wave dispersion, teleseismic traveltime and normal-mode splitting function measurements. *Geophys. J. Int.*, 184(3): 1223–1236, 2011. doi: 10.1111/j.1365-246x.2010.04884.x.
- Rodgers, A. J., Krischer, L., Afanasiev, M., Boehm, C., Doody, C., and Simmons, N. Adjoint Waveform Tomography for Crustal and Upper Mantle Structure of the Middle East and Southwest Asia for Improved Waveform Simulations Using Openly Available Broadband Data. *Bull. Seismol. Soc. Am.*, 2024. doi: <https://doi.org/10.1785/0120230248>.
- Rovden, L. The tectonic expression of slab pull at continental convergent boundaries. *Tectonics*, 12(2):3, 1993. doi: 10.1029/92tc02248.
- Sandvol, E., Seber, D., Barazangi, M., Vernon, F., Mellors, R., and Al-Amri, A. Lithospheric seismic velocity discontinuities beneath the Arabian Shield. *Geophys. Res. Lett.*, 25:2873–2876, 1998. doi: 10.1029/98gl02214.
- Sanfilippo, A., Cai, M. Y., Jácome, A. P. G., and Ligi, M. *Geochemistry of the Lunayyir and Khaybar Volcanic Fields (Saudi Arabia): Insights into the Origin of Cenozoic Arabian Volcanism*, pages 389–415. Springer International Publishing, Cham, 2019. doi: 10.1007/978-3-319-99408-6_18.
- Schaeffer, A. J. and Lebedev, S. Global shear speed structure of the upper mantle and transition zone. *Geophys. J. Int.*, 194:417–449, 2013. doi: 10.1093/gji/ggt095.
- Schettino, A., Macchiavelli, C., Pierantoni, P. P., Zanoni, D., and Ra-

- sul, N. Recent kinematics of the tectonic plates surrounding the Red Sea and Gulf of Aden. *Geophys. J. Int.*, 207:457–480, 2016. doi: 10.1093/gji/ggw280.
- Sen, P., Temel, A., and Gourgaud, A. Petrogenetic modeling of Quaternary post-collisional volcanism: a case study of central and eastern Anatolia. *Geol. Mag.*, 141:81–98, 2004. doi: 10.1017/S0016756803008550.
- Şengör, A., Görür, N., and Şaroğlu, F. Strike-slip faulting and related basin formation in zones of tectonic escape: Turkey as a case study. In *Strike-Slip Deformation, Basin Formation, and Sedimentation*, Kevin T. Biddle, Nicholas Christie-Blick. Special Publications of SEPM, 1985. doi: <https://doi.org/10.21110/pec.85.37.0211>.
- Shapiro, N. M. and Ritzwoller, M. H. Monte-Carlo inversion for a global shear-velocity model of the crust and upper mantle. *Geophysical Journal International*, 151:88–105, 2002. doi: 10.1046/j.1365-246x.2002.01742.x.
- Shedlock, K. M., Giardini, D., Grunthal, G., and Zhang, P. The GSHAP global seismic hazard map. *Seismological Research Letters*, 71(6):679–686, 2000. doi: 10.1785/gssrl.71.6.679.
- Simmons, N. A., Myers, S. C., Johannesson, G., and Matzel, E. LLNL-G3Dv3: Global P wave tomography model for improved regional and teleseismic travel time prediction. *J. Geophys. Res.*, 117 (B10), 2012. doi: 10.1029/2012jb009525.
- Simmons, N. A., Myers, S. C., Morency, C., Chiang, A., and Knapp, D. R. SPiRaL: A Multiresolution Global Tomography Model of Seismic Wave Speeds and Radial Anisotropy Variations in the Crust and Mantle. *Geophysical Journal International*, 227(2): 1366–1391, Nov. 2021. doi: 10.1093/gji/ggab277.
- Sonder, L. J. and England, P. C. Effects of a temperature-dependent rheology on large-scale continental extension. *Journal of Geophysical Research: Solid Earth*, 94(B6):7603–7619, 1989. doi: 10.1016/0148-9062(90)90013-r.
- Spakman, W., Wortel, M., and Vlaar, N. The hellenic subduction zone: A tomographic image and its geodynamic implications. *Geophysical Research Letters*, 15:60–63, 1988. doi: 10.1029/gl015i001p00060.
- Sukhovich, A., Bonnieux, S., Hello, Y., Irisson, J.-O., Simons, F. J., and Nolet, G. Seismic monitoring in the oceans by autonomous floats. *Nature Communications*, 6(1):8027, 2015. doi: 10.1038/ncomms9027.
- Tang, Z., Julià, J., Zahran, H., and Mai, P. M. The lithospheric shear-wave velocity structure of Saudi Arabia: young volcanism in an old shield. *Tectonophysics*, 680:8–27, 2016. doi: 10.1016/j.tecto.2016.05.004.
- Tang, Z., Mai, P. M., Chang, S.-J., and Zahran, H. Evidence for crustal low shear-wave speed in western Saudi Arabia from multi-scale fundamental-mode Rayleigh-wave group-velocity tomography. *Earth and Planetary Science Letters*, 495:24–37, 2018. doi: 10.1016/j.epsl.2018.05.011.
- Tang, Z., Mai, P. M., Julià, J., and Zahran, H. Shear velocity structure beneath Saudi Arabia from the joint inversion of P and S wave receiver functions, and Rayleigh wave group velocity dispersion data. *Journal of Geophysical Research: Solid Earth*, 124 (5):4767–4787, 2019. doi: 10.1029/2018jb017131.
- Tape, C., Liu, Q., Maggi, A., and Tromp, J. Adjoint tomography of the southern California crust. *Science*, 325(5943):988–992, 2009. doi: 10.1126/science.1175298.
- Tarantola, A. Inversion of seismic reflection data in the acoustic approximation. *Geophysics*, 49(8):1259–1266, 1984. doi: 10.1190/1.1441754.
- Tavakoli, B. and Ghafory-Ashtiany, M. Seismic hazard assessment of Iran. *Annali Di Geofisica*, 42(6):1013–1021, 1999. doi: 10.4401/ag-3781.
- Tian, Y., Hung, S.-H., Nolet, G., Montelli, R., and Dahlen, F. A. Dynamic ray tracing and traveltimes corrections for global seismic tomography. *Journal of computational physics*, 226(1):672–687, 2007. doi: 10.1016/j.jcp.2007.04.025.
- Tkalčić, H., Pasyanos, M. E., Rodgers, A. J., Gök, R., Walter, W., and Al-Amri, A. A multistep approach for joint modeling of surface wave dispersion and teleseismic receiver functions: Implications for lithospheric structure of the Arabian Peninsula. *Journal of Geophysical Research: Solid Earth*, 111(B11), 2006. doi: 10.1029/2005JB004130.
- Trampert, J., Deschamps, F., Resovsky, J., and Yuen, D. Probabilistic tomography maps chemical heterogeneities throughout the lower mantle. *Science*, 306(5697):853–856, 2004. doi: 10.1126/science.1101996.
- van der Lee, S. and Nolet, G. Upper mantle S velocity structure of North America. *J. Geophys. Res.*, 102(B10):22815–22838, 1997. doi: 10.1029/97JB01168.
- Viltres, R., Jónsson, S., Alóthman, A. O., Liu, S., Leroy, S., Masson, F., Doubré, S., and Reilinger, R. Present-day motion of the Arabian plate. *Tectonics*, 41:e2021TC007013, 2022. doi: <https://doi.org/10.1029/2021TC>.
- Voronin, S., Mikesell, D., Slezak, I., and Nolet, G. Solving large tomographic linear systems: size reduction and error estimation. *Geophysical Journal International*, 199(1):276–285, 2014. doi: 10.1093/gji/ggu242.
- Wei, W., Zhao, D., Wei, F., Bai, X., and Xu, J. Mantle Dynamics of the Eastern Mediterranean and Middle East: Constraints From P-Wave Anisotropic Tomography. *Geochemistry, Geophysics, Geosystems*, 20:4505–4530, 2019. doi: 10.1029/2019GC008512.
- Weinstein, Y., Navon, O., Altherr, R., and Stein, M. The Role of Lithospheric Mantle Heterogeneity in the Generation of Plio-Pleistocene Alkali Basaltic Suites from NW Harrat Ash Shaam (Israel). *Journal of Petrology*, 47(5):1017–1050, 2006. doi: 10.1093/petrology/egl003.
- Witek, M., Lee, S.-M., Chang, S.-J., and van der Lee, S. Waveform inversion of large data sets for radially anisotropic Earth structure. *Geophys. J. Int.*, 232:1311–1339, 2023. doi: 10.1093/gji/ggac393.
- Woodhouse, J. and Wong, Y. Amplitude, phase and path anomalies of mantle waves. *Geophys. J. R. astr. Soc.*, 87:753–773, 1986. doi: 10.1111/j.1365-246X.1986.tb01970.x.
- Wortel, M. and Spakman, W. Subduction and slab detachment in the Mediterranean-Carpathian region. *Science*, 290:1910–1917, 2003. doi: 10.1126/science.290.5498.1910.
- Zhu, H., Bozdağ, E., Peter, D., and Tromp, J. Structure of the European upper mantle revealed by adjoint tomography. *Nature Geoscience*, 5(7):493, 2012. doi: 10.1038/ngeo1501.

The article *P-Wave Arrival-Time Tomography of the Middle East Using ISC-EHB and Waveform Data* © 2025 by Ebru Bozdağ is licensed under CC BY 4.0.